Preprint Cambridge Centre for Computational Chemical Engineering ISSN 1473 – 4273

The role of oxygenated species in the growth of graphene, fullerenes and carbonaceous particles

Gustavo Leon[1], Jacob W. Martin[2], Eric J. Bringley[1], Jethro Akroyd[1,2], Markus Kraft[1,2,3]

released: April 12, 2021

[1] Department of Chemical Engineering
and Biotechnology
University of Cambridge
Philippa Fawcett Drive
Cambridge, CB3 0AS
United Kingdom

[2] CARES
Cambridge Centre for Advanced
Research and Education in Singapore
1 Create Way
CREATE Tower, #05-05
Singapore, 138602

[3] School of Chemical
and Biomedical Engineering
Nanyang Technological University
62 Nanyang Drive
Singapore, 637459

Preprint No. 269

UNIVERSITY OF CAMBRIDGE

Keywords: Graphene, Fullerenes, Carbonaceous particles, Kinetic Monte Carlo model

Edited by
Computational Modelling Group
Department of Chemical Engineering and Biotechnology
University of Cambridge
Philippa Fawcett Drive
Cambridge, CB3 0AS
United Kingdom

E-Mail: mk306@cam.ac.uk
World Wide Web: https://como.ceb.cam.ac.uk/

Abstract

The growth of carbonaceous materials was studied using a Kinetic Monte Carlo model that captures the growth and oxidation of six-member and partially-embedded five-member rings. A novel algorithm was used to resolve the migration of partially-embedded five-member rings around the edges of molecules. Circumcoronene molecules were grown at 1500 K and 1 atm in the presence of varying mole fractions of atomic and molecular oxygen and constant mole fractions of hydrogen and acetylene. The parameter space of the study covered the mole fraction of atomic and molecular oxygen in the ranges: $10^{-8} \leq X_{\mathrm{O}} \leq 10^{-1}$ and $10^{-6} \leq X_{\mathrm{O}_2} \leq 10^{-1}$. Four regions of carbon growth associated with different carbonaceous products were identified. Graphene was formed in the presence of high mole fractions of atomic oxygen $\left(10^{-4} < X_{\mathrm{O}} \leq 10^{-2}\right)$. Fullerenes were formed in the presence of low mole fractions of atomic oxygen and high mole fractions of molecular oxygen $\left(X_{\mathrm{O}} \leq 10^{-4}\right.$ and $\left.10^{-2} < X_{\mathrm{O}_2} \leq 10^{-1}\right)$. Low mole fractions of both atomic and molecular oxygen $\left(X_{\mathrm{O}} \leq 10^{-4}\right.$ and $\left.X_{\mathrm{O}_2} \leq 10^{-2}\right)$ resulted in structures that became curved as time progressed. The highest mole fractions of atomic oxygen $\left(X_{\mathrm{O}} > 10^{-2}\right)$ produced small structures due to oxidation of the molecules. The production and consumption of partially-embedded five-member rings appear to explain the formation of the observed structures. The oxidation of partially-embedded five-member rings leaves behind armchair sites that grow to form large and flat structures that resemble graphene. Formation and subsequent embedding of partially-embedded five-member rings result in curved structures that resemble fullerenes.

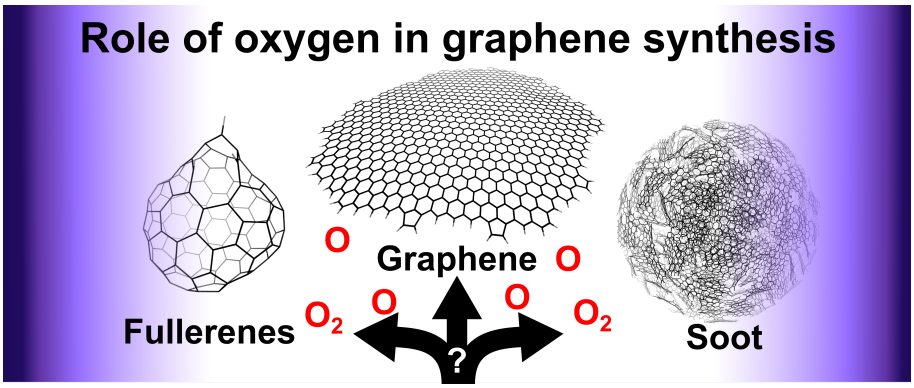

Highlights

- Kinetic Monte Carlo simulations of carbonaceous materials.
- Graphene is produced in the presence of atomic oxygen.
- Fullerenes are produced in the presence of molecular oxygen.
- Partially-embedded five-member rings control curvature of carbonaceous material.

Contents

1 Introduction

The gas phase synthesis of carbonaceous materials is a low cost scalable approach for generating a range of useful products. Carbonaceous particles in the form of carbon blacks can be produced under adequately controlled conditions [99]. Graphene, a large single layer of six-member rings, and fullerenes, closed cage molecules containing alternating five- and six-member rings, can also be produced under specific conditions. Both have many novel applications [13, 29, 60, 62]. Under other conditions, undesirable products like soot are produced. This material, which is another type of carbonaceous particle, is a human health concern and an atmospheric pollutant [94]. The effect of the chemical environment on the formation of carbonaceous particles, fullerenes and graphene is still not fully understood.

Carbonaceous particles, fullerenes and graphene can be produced simultaneously under different conditions. Carbonaceous particles are primarily formed from polycyclic aromatic hydrocarbons (PAHs) produced in oxygen deficient environments such as flames or pyrolysis reactors. There is strong evidence that the interaction of two PAHs leads to the inception of carbonaceous particles, but the identity of these PAHs, and the nature of their interactions, remain elusive [94]. Fullerenes can be produced alongside carbonaceous particles in arc discharge reactors [10]. Fullerenes can also be produced in regions of high temperature [34] and in the presence of oxidising species [32, 38] in low pressure benzene [34] and acetylene [100] flames. Fullerenes are thought to share common intermediates with carbonaceous particles that, instead of gaining mass, embedded five-member rings until the structure becomes fully curved [34]. Graphene can also be produced alongside carbonaceous particles in the gas phase of plasma reactors among other methods [70]. In one setup, ethanol and argon are used in a microwave plasma reactor [4, 15–17, 61, 88, 89]. The presence of oxygen in the precursor was found to be necessary to produce significant amounts of graphene [16]. In another setup, mixtures of methane, hydrogen and argon have been used to produce graphene in a microwave plasma [6, 83] or an arc-discharge plasma at different pressures [93]. In this case, the yield of graphene was reported to increase with increasing hydrogen content in the mixture [83]. In non-plasma conditions, large molecules that resemble graphene have been detected alongside carbonaceous particles in low pressure acetylene flames [100].

The surface growth of carbonaceous materials in a chemical environment is typically described by the hydrogen-abstraction acetylene-addition mechanism, better known as HACA [22] mechanism. This reaction model has been repeatedly used to study the surface growth of carbonaceous particles without discriminating the local chemical structure involved in each reaction [1, 23, 43, 79]. Resolving the local chemical structure, commonly referred to as *sites*, has been shown to be necessary to predict the morphology of carbonaceous products [76]. For example, an acetylene addition can produce either a five- or a six-member ring depending on the site where the reaction takes place [26].

The interactions between carbonaceous materials and oxygenated species have been extensively studied, most typically in combustion experiments. Early experiments on carbon rods with molecular oxygen (O_2) showed that carbonaceous materials present different types of reactive site, resulting in the development the Nagle-Strickland-Constable (NSC) model [92]. Neoh and collaborators showed that in low concentrations of molecular oxy-

gen, oxidation appears to be dominated by hydroxyl radical (OH) [21, 67, 68], and that atomic oxygen (O) is unlikely to be a significant oxidiser in typical flame conditions. However, atomic oxygen has been detected in plasma reactors [39, 86] and in significant concentrations in plasma assisted combustion experiments [41]. These three species appear to play different roles in the oxidation of carbon materials. Molecular oxygen appears to be responsible for the oxidation of carbonaceous particles from the inside of the particles, while hydroxyl radical is associated with surface oxidation [28, 30, 64, 66]. Atomic oxygen has been suggested to contribute to the oxidation of resonantly stabilised radicals [25] as well as producing epoxy and ether groups on the basal planes of PAHs [48]. Those oxygenated groups possibly explain the different oxidation rates observed in recent oxidation experiments of carbon black with molecular and atomic oxygen [64].

Modelling the surface growth and oxidation of carbonaceous materials using kinetic models is challenging. The large number of individual species present in a reactive environment result in a large number of equations to be solved. Two types of model have been used to address this issue. Semi-empirical models have been extensively used to study the surface growth and oxidation of carbonaceous particles [1, 7, 23, 27, 30, 33, 43, 51, 79]. Even though these models reproduce some of the integral properties of carbonaceous particles (*e.g.* volume fraction [79]), they do not resolve the structural transformations of the molecules present in the material. In contrast to this, detailed particle models keep track of the sites available on a molecular edge. The reactions in this kind of model represent the transformation of individual surface sites instead of the full molecule. Detailed particle models typically use a Kinetic Monte Carlo (KMC) method to simulate the reactions occurring at individual sites. These are commonly known as KMC models. These models have been used to study the growth of graphene sheets [24, 102, 103], the formation of carbonaceous particles [76, 105] and the growth of particle precursors [47, 50].

Detailed models have been used to study the interaction of oxygenated and graphenic molecules. Frenklach and collaborators [19, 84, 85] used a KMC model to study the oxidation of different rings on graphene edges. Their results suggest that molecular oxygen and hydroxyl radical are responsible for the oxidation of six-member rings via the decomposition of oxyradicals. This reaction produces either a five-member ring or a partially-embedded five-member ring. They also showed that atomic oxygen is likely to be responsible for the oxidation of partially-embedded five-member rings [25]. The oxidation of six-member rings and partially-embedded five-member rings by different species is shown in Scheme 1. Other detailed models have focused on the formation of oxygenated groups in molecules that are precursors for carbonaceous particles [20, 81, 96, 97]. These studies suggest that oxygenated species can enhance the growth of carbonaceous materials by creating additional types of ring and types of site in the material.

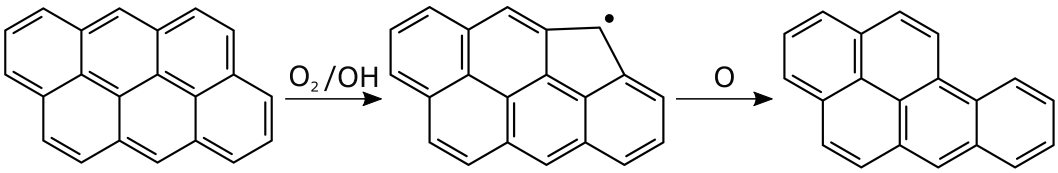

Scheme 1: *Species associated with the oxidation of six-member rings [84] and partially-embedded five-member rings [25].*

Partially-embedded five-member rings play an important role in the growth and oxidation of graphene, fullerenes and carbonaceous particles. Frenklach and collaborators suggested that these rings participate in the growth of graphene sheets by creating additional sites where six-member rings can grow [102]. Once formed, these rings participate in transformation processes that change the morphology of the structure. These are illustrated in Scheme 2. Firstly, partially-embedded five-member rings are able to migrate around the edge facilitated by an hydrogen abstraction reaction. This process allows the rings to be positioned on either the edge or the corner of molecules. However, the kinetics of the migration reaction favour the edge position [104]. Secondly, rings occupying an edge position can become fully-embedded leading to the formation of curved polycyclic aromatic hydrocarbons (cPAHs) [102, 105, 106]. Recently, the recombination of partially-embedded five-member rings and neighbouring seven-member rings has been suggested as a possible mechanism for the formation of graphenic structures [44, 57].

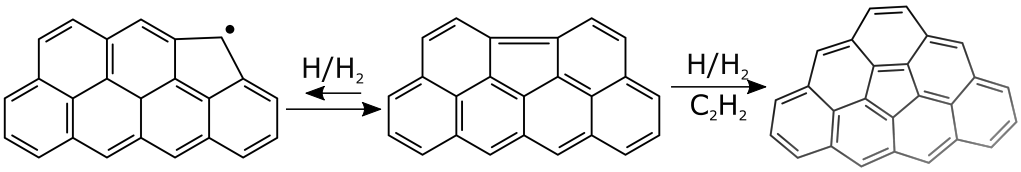

Scheme 2: *Migration and embedding of partially-embedded five-member rings [104].*

The morphology of PAHs is also thought to play an important role in the inception of carbonaceous particles. Recently, two types of radical have been suggested as possible species that could participate in inception processes. First, delocalised π-radicals, which are associated with an odd number of six-member rings [42], delocalise their radical behaviour around the molecular structure giving them additional stability at high temperatures [40]. Second, localised π-radicals [54], which localise their radical character around edge five-member rings and partially-embedded five-member rings. Both types of radical have been suggested to form stable bonds with other PAHs and rate constants for these processes have been calculated [54, 58, 59, 71]. Species with all of these structures have been experimentally observed in carbonaceous particles with different levels of hydrogen content and embedding using atomic force microscopy [11].

The interactions between oxygenated species and different carbonaceous materials have been studied mostly in combustion experiments. However, few studies have focused on conditions that favour the production of materials like graphene or fullerenes. A systematic study on the combined effect of surface growth in the presence of different oxygenated species is still missing.

The **purpose of this paper** is to investigate the effect of the oxygenated species on the formation of carbonaceous particles, fullerenes and graphene. A detailed KMC model is used to simulate the oxidation and growth of molecules in the presence of constant mole fractions of hydrogen and acetylene, and varying mole fractions of atomic and molecular oxygen. Two improvements are made to the model. First, the model is expanded to include the oxidation of partially-embedded five-member rings and six-member rings with rates calculated using a steady-state approximation. Second, a new numerical algorithm is introduced for the efficient simulation of the migration of partially-embedded five-member rings whilst retaining accurate growth and oxidation rates.

2 Methodology

2.1 Kinetic Monte Carlo model

Kinetic Monte Carlo models are useful to study the growth and oxidation of carbonaceous materials because they keep track of the sites that determine the reactivity of the molecules. These sites are allowed to react based on a set of reaction rules that are assumed to be a function of the site type. This gives these models the ability explore the transformation of different structures beyond typical gas phase chemical kinetic mechanisms.

In this work we use the *MOpS Particle Simulator* [12] to track the evolution of molecules in different chemical environments. The details of the model have been described previously [50]. In this work we improve the model by adding new processes for the oxidation of partially-embedded five-member rings and six-member rings using published rates from the literature [19, 25, 84]. The numerical performance of the model is also improved by including a new algorithm to describe the migration of partially-embedded five-member rings more efficiently. The algorithm was developed to be exact (*i.e.* it has no effect on the results calculated by the model), yet reduced computational times by more than an order of magnitude for all simulated cases. A complete description of the individual reactions, the process rates and the new migration algorithm is given in Appendix A.

2.2 Parameter space

Most detailed models have focused on the growth and oxidation of carbonaceous materials in isolated conditions [25, 84, 85]. The few studies that have considered the competition between growth and oxidation have done so in the context of combustion [20, 81, 96, 97]. A systematic parameter sweep to investigate the competition between growth and oxidation is still missing in the literature. To begin to address this gap, the chemical conditions selected in this work have been chosen to consider a constant potential for the growth of carbonaceous materials while varying the potential for both the oxidation of six-member rings and partially-embedded five-member rings.

The oxidation of six-member rings is dominated by two species: molecular oxygen and hydroxyl radicals. However, hydroxyl radicals participate in hydrogen abstraction reactions [2, 8, 65] that promote surface growth. Molecular oxygen has a high energy barrier for the same reaction [25]. For this reason, molecular oxygen was selected for this study. Atomic oxygen was selected as a second oxidising species because it is known to attack partially-embedded five-member rings.

It is desired to study conditions that are relevant to a wide range of experimental scenarios including fuel-rich flames, plasma and pyrolysis reactors. The parameter space therefore spans several orders of magnitude. The conditions used in the study are as follows: The mole fractions of species that contribute to growth were held constant at $X_{\mathrm{H}} = 0.01$ and $X_{\mathrm{H_2}} = X_{\mathrm{C_2H_2}} = 0.1$. These conditions have been widely used to study typical growth environments [57, 75, 102]. Likewise, temperature and pressure were held constant at 1500 K and 1 atm and the simulation time held constant at 5 ms, consistent with previous

studies [57, 75, 84, 102]. The mole fractions of atomic and molecular oxygen were varied in log-scaled intervals covering the ranges $10^{-8} \leq X_{\mathrm{O}} \leq 10^{-1}$ and $10^{-6} \leq X_{\mathrm{O}_2} \leq 10^{-1}$. The balance of the reaction mixture was argon.

The KMC model was used to simulate the oxidation and growth of an ensemble of 300 circumcoronene ($C_{54}H_{18}$) molecules at each condition. The interactions between multiple molecules was not considered.

3 Results and discussion

3.1 Regions of carbon growth

The growth of the molecules resulted in different morphologies in the different chemical environments sampled by the parameter space. However, small variations in the mole fractions of molecular and atomic oxygen resulted in similar structures. This allowed us to divide the parameter space in four regions of carbon growth, where each region is associated with the observation of different carbonaceous structures: (1) large cPAHs, (2) small cPAHs, (3) large flat molecules, and (4) small molecules.

Figure 1 shows the average number of carbons observed in each molecule at the end of each simulation. The edges of the four regions of carbon growth are indicated with dashed lines. Experimental data for flames that produce carbonaceous particles [20, 67], fullerenes [55] and large flat molecules that resemble graphene [101] are shown (and are joined by continuous lines to guide the eye). Symbols are only shown for conditions that had sufficient hydrogen and acetylene to sustain the growth of carbonaceous structures. The geometry of representative molecules sampled from each region are also shown. The geometry of the full set of molecules is available in the Research Data associated with this work.

Region 1 (bottom left of Fig. 1) encompasses the lowest mole fractions of atomic and molecular oxygen, $10^{-8} \leq X_{\mathrm{O}} \leq 10^{-4}$ and $10^{-6} \leq X_{\mathrm{O}_2} \leq 10^{-2}$. The molecules in Region 1 contained an average of 300 carbon atoms. The molecules were mostly flat at early times, but became curved as simulations progressed. This can be seen in the representative structures in Fig. 1. Although the observed structures were large cPAHs, the main product in Region 1 will be carbonaceous particles. There is strong evidence that carbonaceous particles are formed by the interaction of two intermediate (and unknown) PAHs [94]. These interactions were not part of the scope of this study and the possibility to form carbonaceous particles was not included in the current model. However, the molecules in this region spend significant time in the reaction environment before becoming curved. During this time the molecules could form carbonaceous particles. Most premixed sooting flames lie in Region 1. The maximum concentrations of molecular and atomic oxygen appear on the upstream side of the flame front, whilst the maximum concentrations of hydrogen and acetylene appear within the flame. This is represented as a movement towards the bottom left of Fig. 1. Two example flames in Fig. 1 are fully contained in Region 1: a sooting acetylene/air flame [20, 80] and the methane/oxygen experiments by Neoh [67]. The latter is included to highlight that oxidation by hydroxyl radicals becomes signifi-

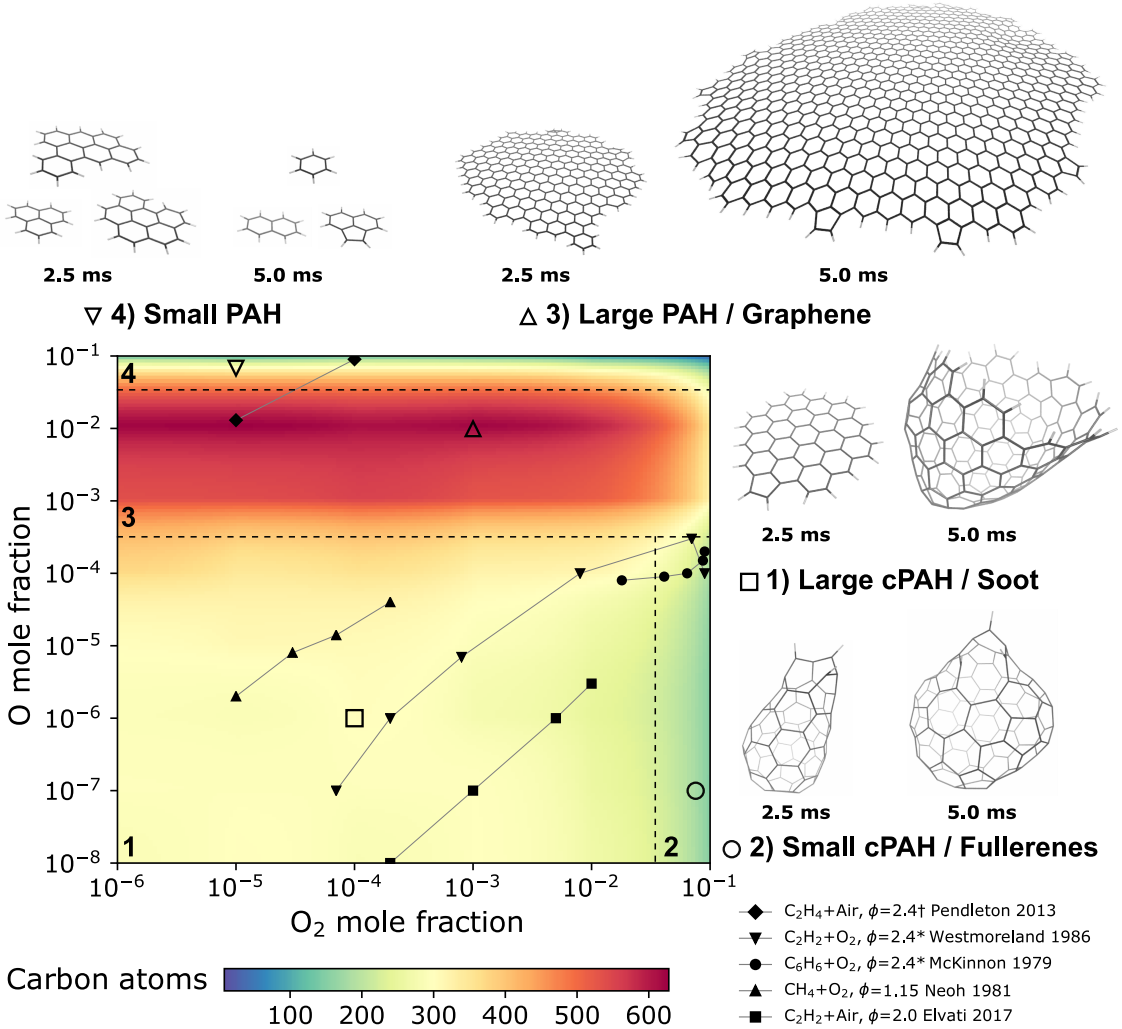

Figure 1: *Average number of carbons in each molecule versus mole fraction of atomic and molecular oxygen. Four regions of carbon growth (1 to 4) are indicated with dashed lines. Representative structures sampled from each region, at conditions indicated with open symbols, are shown. Experiments for which it is possible to estimate the mole fractions of atomic and molecular and oxygen are also shown. These correspond to: (♦) plasma ignition experiment [74], (▼) acetylene/oxygen low pressure flame [101], (●) benzene/oxygen low pressure flame [55], (▲) methane/oxygen flame [68] and (■) ethylene/air sooting flame [20]. Plasma ignition experiment is indicated with a dagger (†). Low pressure conditions (2.7kPa) are indicated with an asterisk (*).*

cant in flames with low mole fractions of molecular oxygen $\left(X_{O_2} < 10^{-5}\right)$. Two other experiments are partially contained in this region and will be discussed below.

Region 2 (bottom right of Fig. 1) encompasses low mole fractions of atomic oxygen and high mole fractions of molecular oxygen, $10^{-8} \leq X_O \leq 10^{-4}$ and $10^{-2} < X_{O_2} \leq 10^{-1}$. The molecules in Region 2 contained an average of 150 carbon atoms. The structures in this

region were highly curved and smaller than those in Region 1. Most of the structures became curved at short times. This can be seen in the representative structures in Fig. 1. The structures in this region resembled open caged fulleroids. Closed caged structures could not be produced in the simulations because no process to close the molecular structure was included in the current model. The interpretation of these observations is that the main product in Region 2 will be fullerenes. These observations are consistent with the experimental evidence presented in Fig. 1, where both carbonaceous particles and fullerenes have been reported in the low pressure acetylene/oxygen [34, 100] and benzene/oxygen flames [36–38] that straddle Region 1 and Region 2.

Region 3 (middle of Fig. 1) encompasses high mole fractions of atomic oxygen and spans the full range of mole fractions of molecular oxygen in Fig. 1, $10^{-4} < X_{\mathrm{O}} \leq 10^{-2}$ and $10^{-6} \leq X_{\mathrm{O}_2} \leq 10^{-1}$. Region 3 is characterised by the highest average number of carbons per molecule: the molecules in Region 3 contained an average of 500 carbon atoms at $X_{\mathrm{O}} = 10^{-3}$ and 600 carbon atoms at $X_{\mathrm{O}} = 10^{-2}$. At high values of molecular oxygen $\left(X_{\mathrm{O}_2} > 10^{-2}\right)$ the molecules in Region 3 showed a lower number of carbons (approximately 300) per molecule due to oxidation. The structures in Region 3 were significantly larger than in the other regions. Most of the molecules were flat throughout the simulation. This can be seen in the representative structures in Fig. 1. The largest molecules were sampled at the higher mole fractions of atomic oxygen $\left(X_{\mathrm{O}} = 10^{-2}\right)$. To our knowledge this is the first time that such large structures have been obtained in a model that allows for the inclusion of curvature as a result of competing oxidation and surface growth. The preferred structure in this region is graphene. The high mole fractions of atomic oxygen that characterise this region make the synthesis of graphene in typical flame conditions unlikely. The only flame that appears to be close to this region is the low pressure acetylene/oxygen flame [100, 101] that reported the presence of large flat molecules in these conditions. However, this observation makes an argument for the production of graphene in other environments. Plasma experiments [*e.g.* 15, 16, 61, 86, 87] are known to form large numbers of oxygen radicals and ions that could perhaps explain the production of graphene. One of the challenges for these processes is to improve the prediction and detection of species formed in the plasma to explain the production of new materials.

Lastly, Region 4 (top of Fig. 1) encompasses the highest mole fractions of atomic oxygen and spans the full range of mole fractions of molecular oxygen in Fig. 1, $X_{\mathrm{O}} > 10^{-2}$ and $10^{-6} \leq X_{\mathrm{O}_2} \leq 10^{-1}$. This region was characterised by a reduction in size of the molecules, despite the presence of hydrogen and acetylene. The molecules in Region 4 were flat and decreased in size during the simulations. This can be seen in the representative structures in Fig. 1.

Two opposite effects are clearly seen on the structures shown in Fig. 1. Molecular oxygen contributes to the integration of curvature while atomic oxygen inhibits it. The mechanism by which these two species lead to one process or the other appears to be related to the production and consumption of partially-embedded five-member rings and is discussed in the following sections.

3.2 Size distributions

The consideration of the average number of carbons per molecule allowed a straightforward comparison between the different regions of carbon growth. However, to have a more complete picture of the predicted structures, it is necessary to analyse the evolution of the size distribution of the sampled species as a function of the chemical conditions.

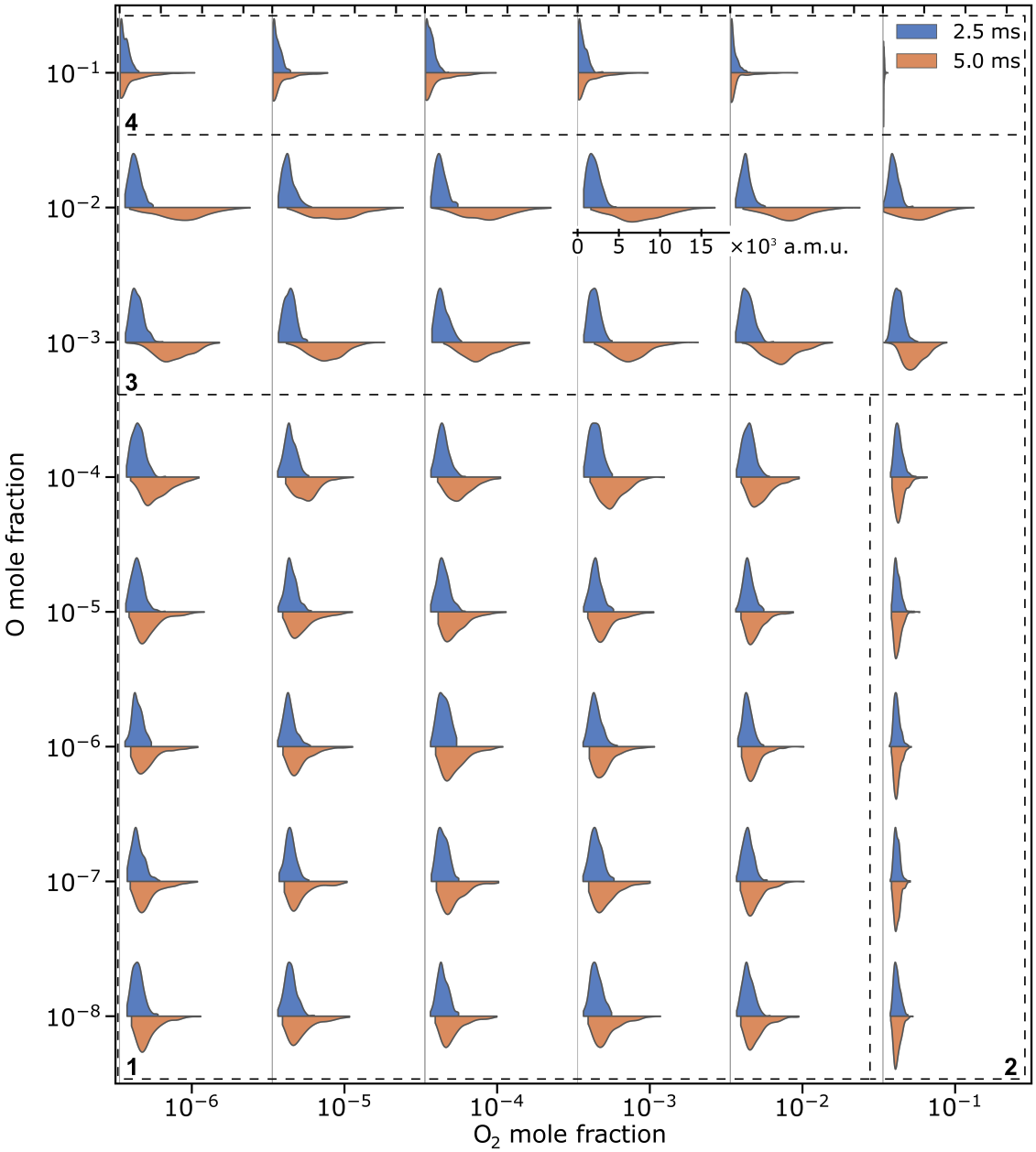

Figure 2: *Molecular mass distribution of molecules versus mole fraction of atomic and molecular oxygen. Simulation times of 2.5 and 5.0 ms are shown in blue and orange. Four regions of carbon growth (1 to 4) are indicated with dashed lines.*

Figure 2 shows the molecular mass distributions of the sampled molecules halfway through

(2.5 ms) and at the end (5.0 ms) of each simulation. Kernel density estimates (calculated using Seaborn with a Gaussian kernel and optimal bandwidth [98]) were used to estimate the continuous distribution functions shown in Fig. 2 from the masses of the molecules sampled by the KMC simulations.

The mass distributions sampled in Region 1 at 2.5 ms were centred around 2,000 a.m.u. with maximum values of approximately 4,000 a.m.u. By 5.0 ms the distributions were centred around 5,500 a.m.u. and presented a tail that extended up to 10,000 a.m.u. The molecules in these tails did not show any particular morphological difference in their structure other than being larger than the other molecules sampled in Region 1. They had a similar number of embedded five-member rings and similarly few hydrogen atoms.

Region 2 showed very similar mass distributions at both simulation times. The distributions were centred at 2,000 a.m.u. with a range extending from 1,000 to 3,000 a.m.u. The similarity of the mass distributions is an indication that the growth of these molecules is not significant after 2.5 ms. This effect can be explained by the decrease in the number of sites available for growth as the structure becomes highly curved.

The mass distributions sampled in Region 3 increased in width during the simulations. At 2.5 ms the distributions were centred around 2,000 a.m.u. with a range extending to approximately 4,000 a.m.u. However, at 5.0 ms the distributions showed ranges extending to 13,000 a.m.u. at $X_{\mathrm{O}} = 10^{-3}$ and extending to more than 16,000 a.m.u. at $X_{\mathrm{O}} = 10^{-2}$. The only exception to these large distributions appeared at $X_{\mathrm{O}_2} = 10^{-1}$, $X_{\mathrm{O}} = 10^{-3}$, where the distribution showed a maximum value of 6,000 a.m.u. The large maximum values are indicative of the growth of large structures. These large structures were observed to be flat or slightly curved. Region 4 showed distributions centred at masses of less than 1,000 a.m.u. but with long tails composed of a few large molecules up to 7,000 a.m.u. in size appearing between 2.5 ms and 5.0 ms. The molecules in the tails of the distribution were smaller than, but otherwise similar to those observed in Region 3 at 5.0 ms.

The residence time has different effects on the mass distribution of the molecules in each region. This can be seen by comparing the distributions of Regions 1 and 3 in Fig. 2. At 2.5 ms the mass distributions in each region are similar. However, the mass distributions are significantly different at 5.0 ms, with Region 3 showing significantly larger molecules. The integration of curvature appears to be crucial in controlling the surface growth of carbonaceous structures. This can be observed in the mass distributions in Region 2, which did not change after 2.5 ms.

3.3 Inclusion of curvature

The curvature of carbonaceous nanostructures is caused by the presence of fully-embedded five-member [102] rings and seven-member [90] rings. In the extreme case, the presence of embedded five-member rings can lead to the formation of closed caged fullerenes. In the absence of embedded five-member and seven-member rings, the molecules take the form of large sheets of six-member rings that resemble graphene.

Figure 3 shows the average number of fully-embedded five-member rings per molecule at 2.5 ms and 5.0 ms. The figure shows that, except at the highest mole fractions of atomic oxygen in Region 4, five-member rings are embedded in the molecules during the

simulations.

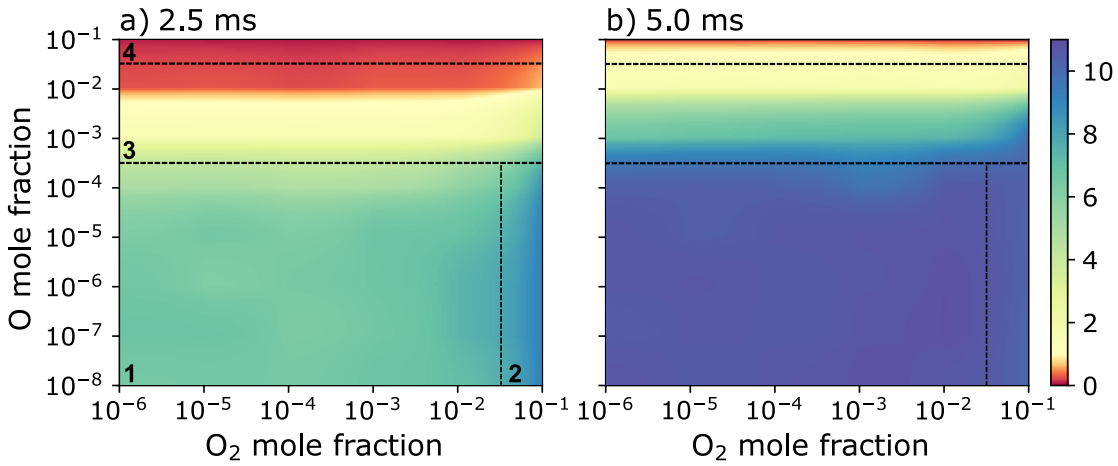

Figure 3: *Average number of fully-embedded five-member rings per molecule at (a) 2.5 ms and (b) 5.0 ms.*

The molecules from Region 1 showed an average of 6 and 11 fully-embedded five-member rings at 2.5 ms and 5.0 ms, respectively. In this region the molecules became increasingly curved during the simulations. At low concentrations of oxygenated species, the molecules steadily embed five-member rings and gain curvature. This has also been observed in earlier work [50].

At 2.5 ms, Region 2 already shows structures that contain an average of 11 embedded five-member rings per molecule, where the first molecule to reach this value was observed after only 1.1 ms. At 5.0 ms, every part of the region has an average of 11 embedded five-member rings. Molecular oxygen in the presence of favourable conditions for surface growth (hydrogen and acetylene) provides an additional pathway for the inclusion of five-member rings. This agrees with the observations of fullerenes sampled from diffusion flames [32] where it was suggested that the presence of molecular oxygen enhances the formation of curved structures.

Region 3 shows a trend similar to that in Regions 1 and 2, but with much slower inclusion of embedded five-member rings. At 2.5 ms the molecules presented an average of only 1 and 0 embedded five-member rings at $X_O = 10^{-3}$ and $X_O = 10^{-2}$ respectively. By 5.0 ms the number of embedded rings had reached 6 and 2 for the same conditions. It appears that for carbonaceous structures subject to HACA growth, the probability of embedding a partially-embedded five-member ring, and thus including curvature, increases with residence time.

The majority of the molecules in Region 4 did not appear to embed curvature at any time. The small structures that characterise this region were not large enough to fully-embed a five-member ring before being oxidised. However, in our study we were unable to find a set of conditions where molecules kept growing without at least some molecules including curvature after some time. This observation, although not surprising, has profound implications for the production of defect free graphene.

3.4 Mechanism for the formation of carbonaceous materials

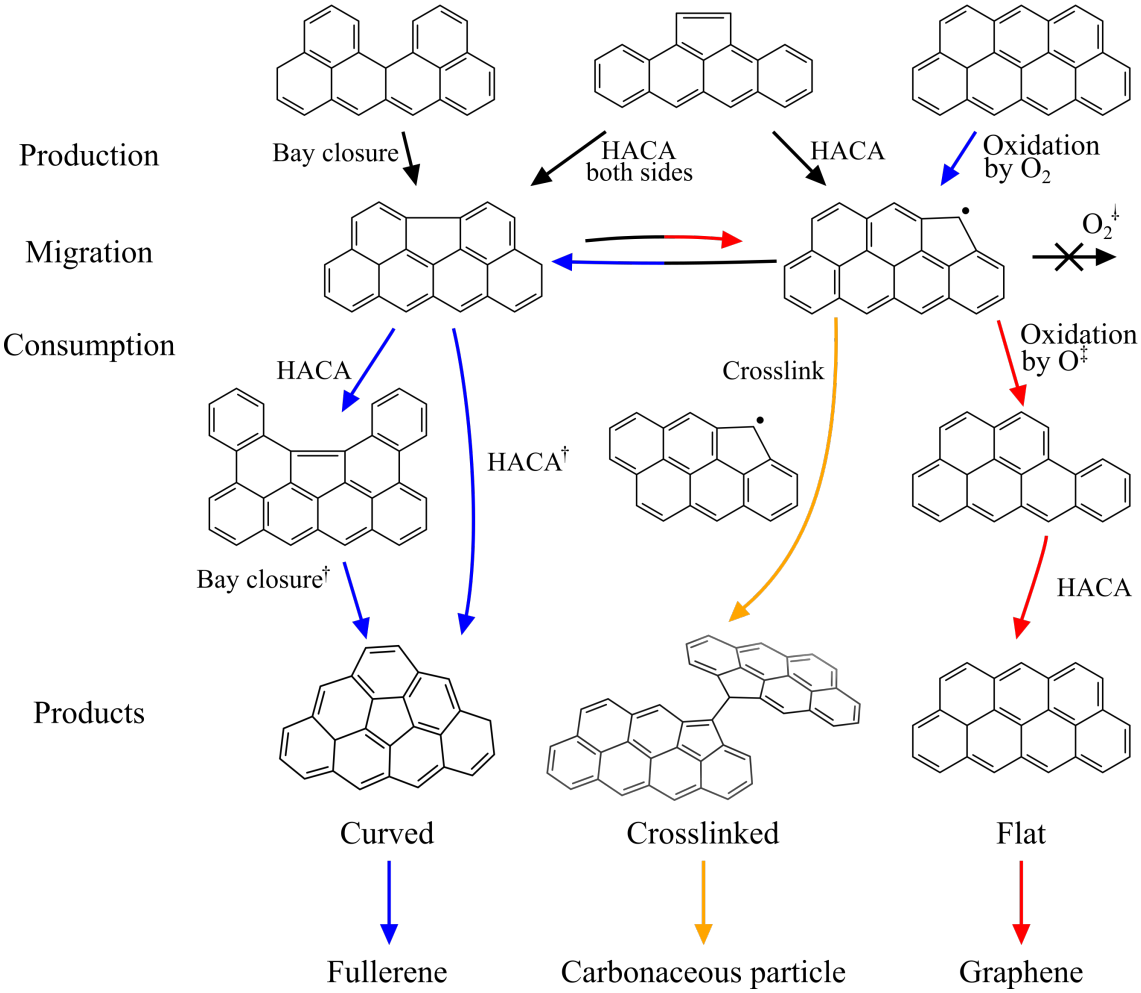

Figure 4: *Mechanism of the formation of carbonaceous particles, fullerenes and graphene from partially-embedded five-member rings. Black arrows show processes that are present in all conditions. Blue arrows show processes that favour the production of fullerenes. Red arrows show processes that favour the production of graphene. Orange arrows show the crosslinking of partially-embedded five-member rings. Crosslinking was not studied in this work but has been suggested by other studies [40, 54].*

Partially-embedded five-member rings play a crucial role in the formation of the different carbon structures discussed in this work. Figure 4 shows processes that produce, transform and consume partially-embedded five-member rings. Under different conditions these processes can explain the formation of graphene, fullerenes and carbonaceous particles. The production of these rings can happen via three processes shown in the top row of the figure: (i) bay closure, (ii) HACA growth neighbouring five-member rings occupying edge positions and (iii) the oxidation of free-edge six-member rings by molecular oxygen. These processes form two different types of partially-embedded five-member

rings (second row of Fig. 4), where the partially-embedded five-member ring can occupy either an edge position (left) or a corner position (right). Once formed, these structures can interconvert via ring migration processes. Previous studies have shown that the edge position is kinetically favoured [104].

The third row of Fig. 4 shows the processes that consume partially-embedded five-member rings. The bay closure and HACA processes (marked with a dagger, †) contribute to the inclusion of curvature via bay-capping of partially-embedded five-member rings occupying edge positions [75, 102, 106]. Oxidation by atomic oxygen (marked with a double dagger, ‡) and the recombination of partially-embedded five-member rings next to seven-member rings (not shown) remove partially-embedded five-member rings occupying corner positions without introducing curvature. A fifth process (crosslinking, orange) is discussed later. The recombination of partially-embedded five-member rings next to seven-member rings (shown in the Appendix, Table A.1, process S27) appeared to be unimportant due to the infrequent sampling of the processes (corresponding to less than 2% of the processes that removed partially-embedded five-member rings at any given point in the parameter space). The oxidation of partially-embedded five-member rings occupying corner positions by molecular oxygen is not favoured (marked with a turned dagger ⸸) [25], whereas oxidation by atomic oxygen (‡) leaves behind an armchair site that can undergo subsequent HACA growth as shown in Fig. 4.

In KMC models, the number of times each process is sampled is proportional to the rate of that process. In this work, the contribution of the chemical environment to growth processes was held constant by maintaining fixed values of the C_2H_2, H and H_2 mole fractions, temperature and pressure, while the contribution to oxidation processes varied as a function of location in the $O-O_2$ parameter space. Figure 5 shows the number of sampled processes that produce (top row of Fig. 4) and consume (third row of Fig. 4) partially-embedded five-member rings across the $O-O_2$ parameter space. The bars have been divided to show the contribution of each process. The number of sampled processes for six-member ring growth are also shown.

The different regions of the parameter space show different behaviours. In Region 1 the formation of partially-embedded five-member rings was dominated by HACA (blue) and bay closure (green) processes. This region also showed an increase in the production of partially-embedded five-member rings via oxidation (red) of six-member rings as the mole fraction of molecular oxygen increased. The consumption of partially-embedded five-member rings in this region was dominated by HACA (blue) and bay closure (green) processes that result in curved structures. The number of six-member ring growth processes (orange) sampled in this region was the second highest, exceeded only by Region 3.

Region 2 showed increased production of partially-embedded five-member rings due to oxidation (red) by molecular oxygen. The consumption of these rings was mainly driven by HACA (blue) and bay closure (green) processes forming fully-embedded five-member rings. This increased production of partially-embedded five-member rings is consistent with previous work [84]. The low number of six-member ring growth processes (orange) sampled in this region is a consequence of the rapid embedding of curvature and the consequent reduction in the number of sites available for further HACA growth.

In Region 3, partially-embedded five-member rings were produced by HACA (blue), bay

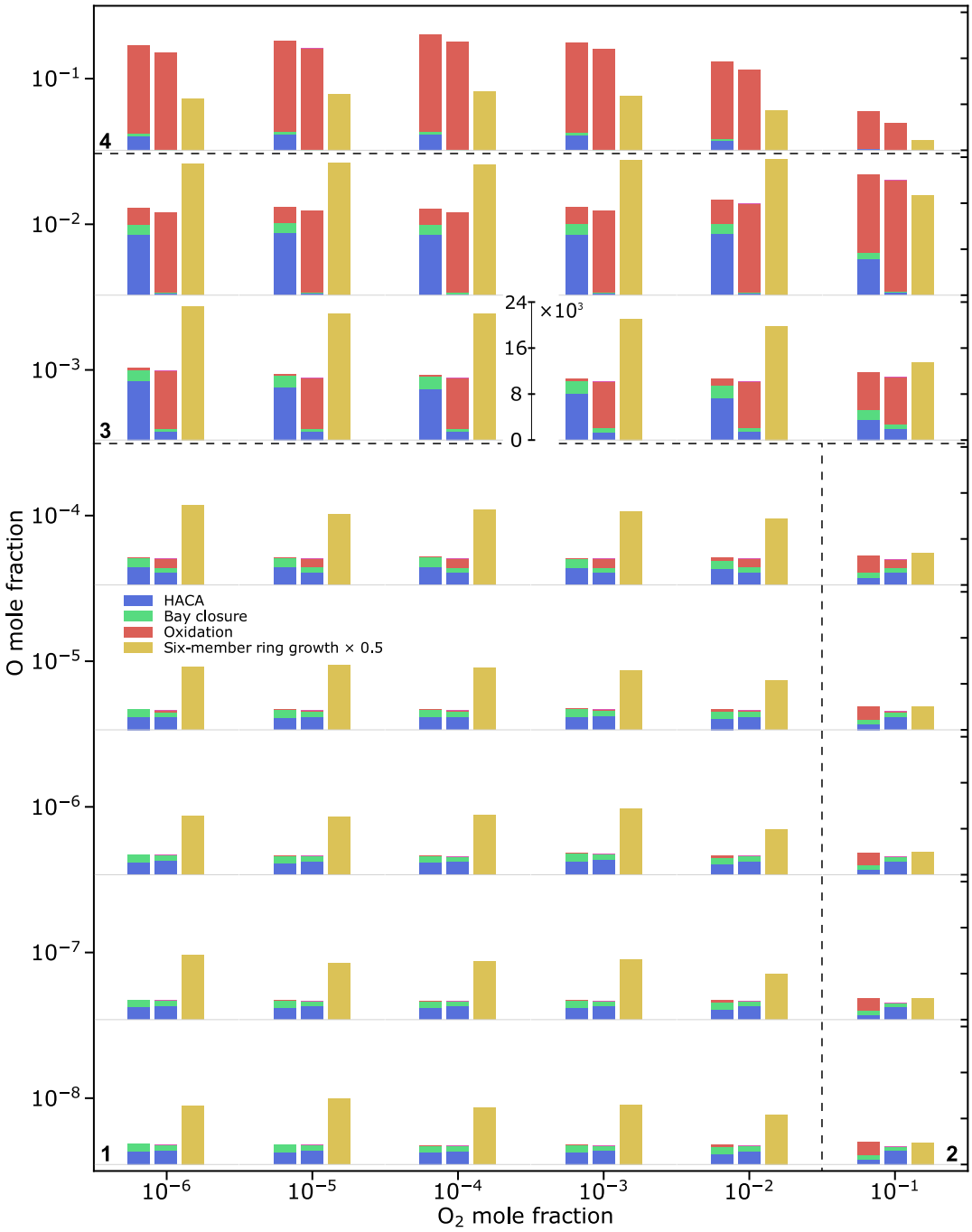

Figure 5: *Number of sampled processes in each simulation of 300 molecules. The first bar in each plot shows processes that produce partially-embedded five-member rings. The second bar shows processes that consume partially-embedded five-member rings. The bars are divided to show the contributions by HACA (blue), bay closure (green) and oxidation (red). The third bar shows processes that produce six-member rings (orange). Four regions of carbon growth (1 to 4) are indicated with dashed lines.*

closure (green) and six-member ring oxidation (red) processes. The number of sampled oxidation processes increased as the mole fraction of molecular oxygen increased. The consumption of partially-embedded five-member rings was mainly due to oxidation (red) by atomic oxygen, with this process becoming more dominant as the mole fraction of atomic oxygen increased. The armchair sites produced by the oxidation (red) of partially-embedded five-member rings by atomic oxygen allow further growth without the inclusion of curvature. This is consistent with the observation that Region 3 sampled the highest number of six-member ring growth processes (orange) of all regions, with the number of sampled processes only notably decreasing at very high mole fractions of molecular oxygen $\left(X_{O_2} > 10^{-2}\right)$. It is possible that atomic oxygen produced in plasma reactors contributes to the formation of graphene following these processes.

Region 4 sampled a large number of oxidation (red) processes that both produced and consumed partially-embedded five-member rings, alongside a significant number of six-member ring growth processes (orange) consistent with the production of armchair sites by the oxidation (red) of partially-embedded five-member rings by atomic oxygen. The net effect was a reduction in the size of the molecules during the simulations in Region 4.

The combination of processes that produce and consume partially-embedded five-member rings provides a possible explanation for the formation of fullerenes and graphene. In the absence of atomic oxygen, high mole fractions of molecular oxygen result in the production of additional partially-embedded five-member rings that can become fully-embedded after migration processes move them to edge positions. This results in curved structures, with an associated decrease in the number of sites that are available for reaction. This reduces the rate of growth and results in conditions that are favourable for the formation of fullerenes. Crosslinking with other carbonaceous molecules may be another process that contributes to the formation of fullerenes [34]. In the presence of atomic oxygen, partially-embedded five-member rings occupying a corner position can be oxidised to produce armchair sites that can subsequently grow via a HACA addition. This results in larger flat molecules that resemble graphene. These processes are indicated in Fig. 4 with blue and red arrows showing processes that we have discussed in connection with the formation of fullerenes and graphene respectively. There is also evidence for the formation of graphene in oxygen-free plasma reactors [6, 83]. This suggests that there must also be other mechanisms that prevent the inclusion of curvature in the molecules. A possible pathway could be the consumption of partially-embedded five-member due to ring enlargements caused by reactions with species that add a single carbon atom (*e.g.* methyl radical) [3]. This process could convert five-member rings into six-member rings.

The orange arrows on Fig. 4 indicate crosslinking processes between (as yet unknown) structures. Although these processes are not simulated in the current KMC model, they are believed to occur during the formation of carbonaceous particles and may be related to the presence of five-member rings. Many structures containing five-member rings have been shown to be able to form localised π-radicals [54]. The structure containing the partially-embedded five-member ring occupying a corner position (right, second row of Fig. 4) is an example of such a radical. It has been shown that the crosslinking of large localised π-radicals (from approximately 400 a.m.u.) results in stable bonded and stacked structures [54], that multiple localised π-radicals are possible within a single structure and that the concentrations of localised π-radicals are potentially significant at 1400–

1500 K [58], leading to the suggestion of localised π-radicals as possible candidates to explain the inception of carbonaceous particles. Under conditions that slowly consume partially-embedded five-member rings (Region 1), as opposed to rapidly embedding the rings (Region 2) or oxidising them (Region 3), the molecules are likely to have enough time to form localised radical sites and interact with other molecules. Both of these observations are consistent with the pressure dependency of the different products: lower pressures drastically reduce the formation of carbonaceous particles, favouring the formation of fullerenes and graphene. This mechanism for the formation of carbonaceous particles via the collision of localised π-radicals needs further investigation.

4 Conclusions

A KMC model was used to study the growth of carbonaceous structures under different chemical conditions. The model includes processes for growth and for the oxidation of six-member rings and partially-embedded five-member rings, and uses a new algorithm for the efficient simulation of the migration of partially-embedded five-member rings around the edge of the molecules. The mole fractions of hydrogen and acetylene were held constant at $X_{\mathrm{H}} = 0.01$ and $X_{\mathrm{H_2}} = X_{\mathrm{C_2H_2}} = 0.1$, whilst the mole fractions of atomic and molecular oxygen were varied in range $10^{-8} \leq X_{\mathrm{O}} \leq 10^{-1}$ and $10^{-6} \leq X_{\mathrm{O_2}} \leq 10^{-1}$. The balance of the reaction mixture was argon.

The model was used to simulate the change in the structure of 300 circumcoronene ($C_{54}H_{18}$) molecules at each set of conditions. It was observed that atomic and molecular oxygen, which preferentially oxidise five-member and six-member rings respectively, have different effects on the size and morphology of the resulting carbonaceous structures. Four different regions of carbon growth, each of which is associated with processes that produce and consume partially-embedded five-member rings, were observed:

- In conditions with significant mole fractions of atomic oxygen $\left(10^{-4} < X_{\mathrm{O}} \leq 10^{-2}\right)$ and the full range of mole fractions of molecular oxygen $\left(X_{\mathrm{O_2}} \leq 10^{-1}\right)$, the oxidation of partially-embedded five-member rings produces armchair sites that participate in further growth processes. This produces large and flat molecules that keep growing as time progresses. This region is associated with the production of graphene.

- In conditions with significant mole fractions of molecular oxygen $\left(X_{\mathrm{O_2}} > 10^{-2}\right)$ and low mole fractions of atomic oxygen $\left(X_{\mathrm{O}} \leq 10^{-4}\right)$, the oxidation of six-member rings produces additional partially-embedded five-member rings that become rapidly embedded and formed highly curved structures. This region is associated with the production of fullerenes.

- In conditions with high mole fractions of atomic oxygen $\left(X_{\mathrm{O}} > 10^{-2}\right)$ and the full range of mole fractions of molecular oxygen $\left(X_{\mathrm{O_2}} \leq 10^{-1}\right)$, the oxidation of both six-member rings and partially-embedded five-member rings resulted in a reduction in the size of the simulated molecules.

- In conditions with low mole fractions of both molecular and atomic oxygen $\left(X_{O_2} \leq 10^{-2} \text{ and } X_O \leq 10^{-4}\right)$ the simulated molecules became curved and grew slowly resulting in molecules with intermediate sizes. The possibility is raised that the slow inclusion of curvature in this region allows the formation of localised π-radicals in partially-embedded five-member rings. These radicals have been suggested to participate in the formation of carbonaceous particles [54].

The regions of carbon growth with low mole fractions of atomic oxygen agree well with known observations of the appearance of carbonaceous particles and fullerenes. The other regions seem unlikely to be observed in typical flame environments. However, processes associated with an increased production of atomic oxygen such as plasma reactors may operate at such conditions. This could contribute to the production of graphene in such processes.

The production and consumption of partially-embedded five-member rings appears to be important in explaining the formation of graphene, fullerenes and carbonaceous particles. These rings have been observed experimentally [11]. Further work is necessary to understand their role with respect to the viability of crosslinking in different chemical environments.

Research data

The source code for the KMC model [12] used in this paper is available on GitHub (`https://github.com/ucam-ceb-como/MOpS`) under an open source licence. All simulated structures are available to download from the University of Cambridge data repository (doi:10.17863/CAM.66055).

5 Acknowledgements

This research was supported by the National Research Foundation, Prime Minister's Office, Singapore under its Campus for Research Excellence and Technological Enterprise (CREATE) programme. GL was funded by a CONACYT Cambridge Scholarship and acknowledges the National Council of Science and Technology and the Cambridge Commonwealth Trust. EJB was funded by a Gates Cambridge Scholarship (OPP1144). MK gratefully acknowledges the support of the Alexander von Humboldt foundation. The authors are grateful to EPSRC (grant number: EP/R029369/1) and ARCHER for financial and computational support as a part of their funding to the UK Consortium on Turbulent Reacting Flows (www.ukctrf.com).

A Appendix

A.1 Reported experimental conditions

This section explains the origin of the experimental data reported in Figure 1 in the main text.

A.1.1 Low pressure benzene/oxygen flame

Low pressure benzene/oxygen/argon flames have been used to study the formation of fullerenes for several decades [5, 32, 36–38]. However, the detection of atomic oxygen in these flames has been difficult due to the abundance of methane [5, 18], which has the same molecular weight as atomic oxygen. Modelling studies [*e.g.* 18, 78] have also not focused on reporting this species.

The closest data available have been taken from McKinnon [55], who studied this flame for pressures ranging between 20 and 40 torr, equivalence ratios (ϕ) ranging between 2.0 and 2.5, and dilutions between 0 and 45%. McKinnon [55] reported molecular oxygen measurements at 40 torr, $\phi = 2.4$ and 10% dilution. Temperatures between 2000 and 2030 K were reported in the regions of the flames that contained mole fractions of molecular oxygen in the range $\left(X_{O_2} \leq 10^{-1}\right)$. Atomic oxygen was not reported for these conditions but equilibrium calculations as a function of temperature and equivalence ratio were reported for a system at 20 torr and 30% dilution. Assuming that these conditions are similar to those reported above ($\phi = 2.4$, $2000 < T < 2030$ K) the equilibrium atomic oxygen mole fractions correspond to $8 \times 10^{-5} < X_O < 2 \times 10^{-4}$.

A.1.2 Low pressure acetylene/oxygen flame

Several low pressure acetylene/oxygen/argon flames have been used to study the formation of carbonaceous particles. Of particular interest is that of Homann and collaborators [100], who used undiluted flames at 20 torr with equivalence ratios between 1.75 and 2.65. They reported the presence of fullerene ions of different sizes as well as large PAHs with more than 400 carbon atoms at an equivalence ratio $\phi = 2.5$ and a laminar flame speed of 42 cm/s. The C/H ratio of the largest PAH molecules was reported to be between 6.0 and 7.0, which suggests the presence of large edges and few fully-embedded five-member rings.

The mole fractions of the gas phase species in these flames were taken from Westmoreland [101], who studied a flame at 20 torr with an equivalence ratio of 2.4 with 5.0% dilution by argon. Westmoreland [101] reported mole fractions for molecular oxygen as a function of height above the burner and estimated mole fractions for atomic oxygen using five different mechanisms that show similar trends and reasonable agreement with each other. Values were taken from those reported from the mechanism by Warnatz (WZ).

A.1.3 Atmospheric ethylene/air plasma ignition

Measuring species generated in plasma conditions is a complicated task that becomes even more difficult in the presence of carbonaceous materials. Most plasma experiments associated with carbonaceous fuels have focused on determining the concentrations of atomic oxygen during the ignition of the flame in the context of plasma assisted combustion. However, even in this case only a few experiments have attempted to measure the concentration of atomic oxygen in fuel rich conditions [41, 69]. In this work we report the results from ignition experiments by Pendleton et al. [74] to estimate the concentration of atomic oxygen in plasma environments. Further work is needed to determine better estimates.

Pendleton et al. [74] used a streamer discharge to create a Gaussian-like voltage waveform lasting for 40 ns. Two-photon absorption laser-induced fluorescence (TALIF) was used to measure the number density of atomic oxygen 8 mm above an atmospheric pressure McKenna burner at the point of igniting the flame. Using premixed ethylene and air at an equivalence ratio of 2.4 and a flame speed of 10 cm/s they reported an oxygen atom number density of 4.5×10^{17} cm^{-3} that decayed to 7.0×10^{16} cm^{-3} as the atomic oxygen was consumed. In a previous work [73] they reported temperatures between 1350 and 1540 K measured using coherent anti-Stokes Raman spectroscopy (CARS). These values imply that the mole fraction of atomic oxygen lies in the range $1.3 \times 10^{-2} < X_{\mathrm{O}} < 9.3 \times 10^{-2}$.

A.1.4 Methane/oxygen burnout experiments

The experiments by Neoh and collaborators [66–68] used a two-flame system. A premixed methane/oxygen flame (equivalence ratio, $\phi = 2.10$) was used to generate carbonaceous particles (soot). The gases and carbonaceous particles (soot) produced in this flame were introduced into a second flame that operated under oxidising conditions with equivalence ratios between 0.85 and 1.15.

The values reported in the main text are from the second flame with an equivalence ratio of 1.15 [68]. Although Neoh et al. [68] do not report the mole fraction of acetylene, the mole fraction of hydrogen for this case was reported to be between 2 and 3%, which is high enough to result in mole fractions of acetylene and hydrogen that are relevant to the current work. The mole fractions for molecular oxygen, atomic oxygen and hydroxyl radical are reported in more detail in [67] for these conditions. These experiments show values as high as $X_{\mathrm{O}_2} = 10^{-2}$, $X_{\mathrm{O}} = 10^{-3}$ in oxidising conditions. The values reported in the main text correspond to values where enough acetylene and hydrogen could be assumed to be present in the burnout experiments.

A.1.5 Atmospheric ethylene/air flame

The atmospheric pressure ethylene/air flame investigated by Salamanca et al. [80] (equivalence ratio, $\phi = 2.01$) was modelled by Elvati et al. [20] using a combination of two mechanisms [14, 53]. The mole fractions of both atomic and molecular oxygen are re-

ported in the supplemental material provided by Elvati et al. [20, Figure S2(a) and (f)]. The concentration of hydrogen and acetylene in the reported domain appear to be sufficient to sustain the growth of carbonaceous materials $(X_{C_2H_2} > 0.01$ and $X_{H_2} > 0.01)$.

A.2 Migration algorithm

The migration algorithm implemented in this work is based on the studies performed by Frenklach and collaborators [102–104]. In their work, the migration of a partially-embedded five-member ring was accurately described as a one-dimensional random walk along the edge of a molecule, where the random walk is terminated when a process that consumes the *random walker* is observed. The rates of the migration processes favour the edge position over the corner position as described in relation to Scheme 2 in the main text.

In the previous version of the KMC model [50], two computational structures are modified every time a process is sampled: First, a site list is updated to maintain a cache of the types and locations of the sites that exist around the perimeter of the molecule. Second, the structure is updated to record the new locations of the carbon and hydrogen atoms in the molecule. In general, both the site list and the structure of the molecule are required for accurate simulation of the growth of the molecule. However, in the case of successive migration steps, it is sufficient to update only the site list. It is only necessary to update the structure when a non-migration process is sampled (or when the migration results in certain structural changes, see Section A.2.2). The rates of the migration processes are such that a partially-embedded five-member ring on a given edge will typically move a number of times before the ring leaves the edge or before a non-migration transformation is sampled, such that updating the structure after each migration process adds significant unnecessary computational cost.

In this work, the KMC model is modified to implement, for the first time, an algorithm that defers the update of the carbonaceous structure whilst successive partially-embedded five-member ring migration processes are sampled. The algorithm keeps track of the number and direction of each partially-embedded five-member ring migration step, such that the structure of the molecule can be recovered whenever it is required for other calculations. The modified algorithm is summarised in Algorithm 1. In the case of random walks of only one step (*i.e.* no deferred migration steps) the modified algorithm reduces to the previous algorithm.

The exactness and computational performance of the modified algorithm were investigated. The previous algorithm was selected as a baseline because the site list and structure of the molecule are updated after each sampled process, ensuring accurate resolution of the migration processes. From this point on we refer to the modified algorithm as the *deferred update* algorithm and the previous algorithm as the *reference* algorithm.

Both algorithms were used to simulate the evolution of 163 representative molecules with varying number of partially-embedded five-member rings selected from our previous work [50]. The simulations used a submechanism that only included migration processes and processes that terminate the migration of partially-embedded five-member rings (Table A.1, processes S18, S19, S22–S27, S30). The simulations used constant mole fractions of $X_{\mathrm{H}} = 0.01$, $X_{\mathrm{H_2}} = X_{\mathrm{C_2H_2}} = 0.1$, $X_{\mathrm{O_2}} = X_{\mathrm{O}} = 0.001$ and a constant temperature and pressure of 1500 K and 1 atmosphere. Ten repetitions of each simulation were performed using different numerical seeds.

Algorithm 1: KMC algorithm with deferred update

Input: State of molecule Q_0 at t_0; Final time t_f.
Output: State of molecule Q_f at t_f.
begin
  $Q \leftarrow Q_0$
  $t \leftarrow t_0$
  deferredMigration $\leftarrow$ *False*
  while $t < t_f$ **do**
    Calculate total rate of surface growth processes:

$$R_{tot}(Q) = \sum_j R_j(Q), \qquad \text{where } R_j(Q) = k_j f_j [\mathrm{A}] N_{site,j}(Q),$$

    where k_j is the rate constant, f_j is the fraction of radical sites, estimated using the steady-state approximation, [A] is the concentration of gas-phase species A and $N_{site,j}(Q)$ is the number of sites that participate in process j.
    Calculate an exponentially distributed waiting time, $\tau \sim \mathrm{Exp}(R_{tot})$.
    Select a process j with probability $P(j) = R_j / R_{tot}$.
    Select a site s_k to perform process j with probability $P(k) = 1/N_{site,j}(Q)$.
    `/* Perform Jump Process` j `*/`
    if $j \in$ MIGRATION **then** `/* A migration process */`
      if deferredMigration = *False* **then** `/* Defer migration process */`
        deferredMigration $\leftarrow$ *True*
        Initialise set of random walkers, $\mathscr{W} = \{w_1, w_2, \ldots, w_{N_w}\}$, `/* One per migrating site */`
        where each random walker is represented as a pair $w_m = (i_m, n_m)$ defined by the initial location of the migrating site i_m and the net number of steps taken during the random walk n_m, such that the current location of migrating site k, described by walker $m(k)$, is $k = i_m + n_m$.
      end
      Look up index of migrating site
      $m \leftarrow m(k)$
      Select migration direction
      Select the landing site for the migration, $s_l \in \{s_{k+1}, s_{k-1}\}$.
      $n_m \leftarrow n_m \pm 1$.
      if go around corner **then** `/* Site moves around the corner */`
        Modify structure – only affected sites
        Add carbon atom to site s_{i_m}. `/* Site now contains six-member ring */`
        Remove carbon atom from s_l. `/* Site now contains five-member ring */`
        Remove site next to s_l. Add site next to s_{i_m}. `/* Update number of sites */`
        Update walker with new migrating site data, $w_m \leftarrow (i_m = l, n_m = 0)$.
      end
      Update sites `/* Rates are accurate */`
      Update the site type of s_k (remove partially-embedded five-member ring). `/* Update site list */`
      Update the site type of s_l (add partially-embedded five-member ring). `/* Update site list */`
      Update neighbouring sites. `/* Sites affect their neighbours */`
    else `/* Not a migration process */`
      if deferredMigration **then**
        Modify structure – update the location of all migration sites
        Add carbon atoms and new sites, update site types for all initial sites s_{i_m} in $\mathscr{W}$.
        Remove carbon atoms and neighbour sites, update site types for all final sites $s_{i_m+n_m}$ in $\mathscr{W}$.
        Update neighbouring sites. `/* Sites affect their neighbours */`
        Optimise structure `/* After all migration processes */`
        deferredMigration $\leftarrow$ *False*
      end
      Perform non-migration jump process
      $Q \leftarrow Q_t$
    end
    $t \leftarrow t + \tau$
  end
  return Q
end

A.2.1 Exactness

Figure A.1 shows the net number of steps taken during the migration of partially-embedded five-member rings simulated using the deferred update algorithm (solid lines) and the reference algorithm (open circles) for representative molecules. Both algorithms sampled the same sequence of processes resulting in the same structures at the same point in each simulation. This demonstrates that the deferred update algorithm is exact in the sense that it produces the correct sites in the migration of partially-embedded five-member rings. The same exact agreement was seen for all repetitions of all 163 tested molecules.

Fig. A.1 also shows the distribution of the locations of the partially-embedded rings after different numbers of migration steps. The distributions were calculated using a kernel density estimate (calculated using Scikit-Learn [72] with a Gaussian kernel and bandwidth = 5.0) for 5000 repetitions of the same molecule using the deferred update algorithm. The distributions confirm that the behaviour described by Frenklach and collaborators [104] is maintained: the migration of a partially-embedded five-member ring follows a one-dimensional random walk. As expected, the distributions are approximately Gaussian, centred on the starting position and become wider with successive steps.

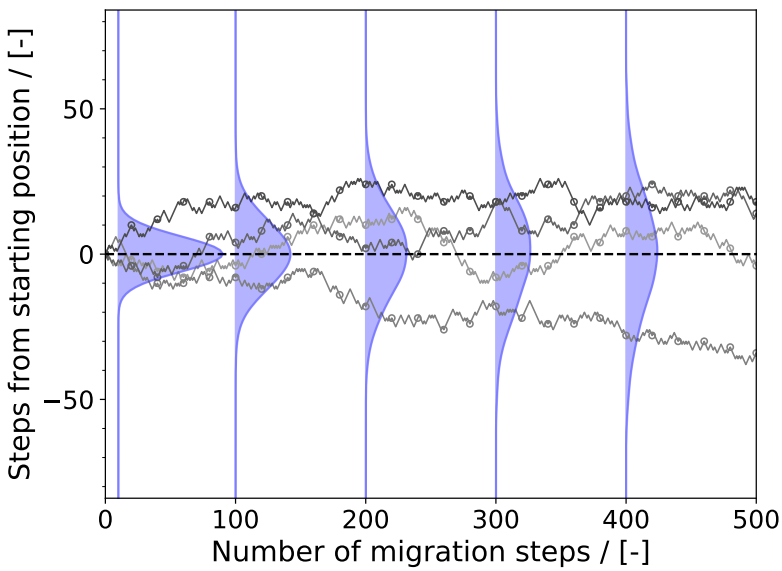

Figure A.1: *Comparison of the net number of steps taken during the migration of partially-embedded five-member rings simulated using the modified KMC model (deferred update algorithm, this work) and the previous KMC model (reference algorithm [50]). Solid lines show the position of the random walker simulated using the deferred update algorithm. Open circles (○) show the position of the random walker simulated using the reference algorithm (structure updated after every step). The distributions shown after 10, 100, 200, 300 and 400 steps were calculated using 5000 repetitions of the deferred update algorithm.*

A.2.2 Computational performance

Figure A.2 shows the computational time spent on the simulation of the migration processes using the deferred update algorithm (circles) and the reference algorithm (crosses). The computational time is proportional to the number of migration steps for the reference algorithm. However, the deferred update algorithm shows two groups of points: random walks where there is a weak dependence between the computational time and the number of migration steps, and random walks where the dependence is similar to that of the reference algorithm.

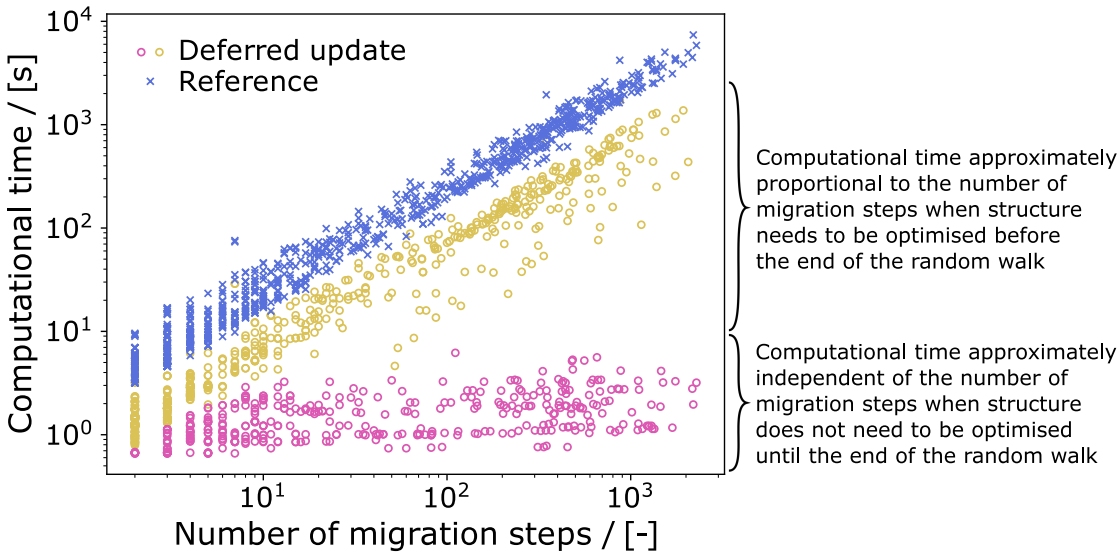

Figure A.2: *Computational time obtained with the updated-deferred algorithm (circles) and with the reference algorithm (crosses). Structures were sampled from the counterflow diffusion flame studied in [50].*

The first group of points corresponds to structures that did not need to be updated until the random walk was finished. The second group of points corresponds to structures that needed to be updated before the end of the random walk. This occurred exclusively in cases where the partially-embedded five-member ring became exposed to the other side of the molecule. This is illustrated in Scheme A.1. The deferred update algorithm identifies this as the creation of an additional random walker on a different edge that could be subject to migration processes. To address this correctly the structure must be updated and optimised before continuing with the random walk. This shows that there are still several possibilities for further improvements in the simulation of migration processes.

The computational time saved by the deferred update algorithm is proportional to the number of steps that are deferred, such that the computational savings are largest when migration processes dominate. Even though it was still necessary to update the structure of some of the molecules mid-migration (see above), the computational savings obtained are significant. The deferred update algorithm was, on average, observed to be two orders of magnitude faster than the reference algorithm.

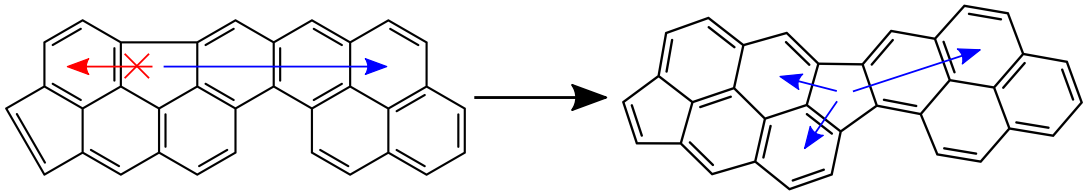

Scheme A.1: *A partially-embedded five-member ring can sometimes become exposed to both sides of a molecule during the simulation of migration processes. Blue arrows show possible directions for the migration.*

A.3 Kinetic Monte Carlo model details

A.3.1 New processes

The model implemented in this work uses the following new processes:

- **Recombination of five- and seven-member rings**.

  The recombination of a partially-embedded five-member ring with a seven-member ring via an azulene–naphthalene rearrangement has been suggested previously [44, 57] and is included using rates from Menon et al. [57] with a steady-state approximation for the radical intermediates. This process only applies to partially-embedded five-member rings adjacent to seven-member rings. (Table A.1, process S27).

- **Oxidation processes**.

  In this work processes for the oxidation of six-member rings and partially-embedded five-member rings have been implemented with rates taken from references [19, 25, 52, 84, 85]. These processes are implemented using a steady-state approximation for the oxygenated intermediates. (Table A.1, processes S28–S30).

  This replaces the processes used in previous versions of the KMC model [76, 105], which used oxidation rates similar to those of the NSC model [92] and the model of Neoh and collaborators [68]. These rates showed acceptable behaviour in the modelling of soot particles but did not allow for the formation of five-member rings by oxidation.

A.3.2 List of Kinetic Monte Carlo jump processes and rates

Tables A.1 and A.2 provide full details of the elementary reaction rate coefficients and the jump processes with their respective rates used in the model.

Table A.1: *Elementary reaction rate coefficients.*

No.	Reaction	$k = AT^n \exp(-E/RT)$[a] A	n	E	References
	Hydrogen abstraction from six-member rings				
1	$C_sR_6{-}H + H \rightarrow C_sR_6^{\bullet} + H_2$	4.570×10^{08}	1.880	14.839	[82]
-1	$C_sR_6^{\bullet} + H_2 \rightarrow C_sR_6 + H$	1.690×10^{04}	2.620	4.559	[82]
2	$C_sR_6{-}H + OH \rightarrow C_sR_6^{\bullet} + H_2O$	5.190×10^{03}	3.040	3.675	[45]
-2	$C_sR_6^{\bullet} + H_2O \rightarrow C_sR_6 + OH$	5.590×10^{00}	3.573	8.659	[45]
3	$C_sR_6^{\bullet} + H \rightarrow C_sR_6{-}H$	4.170×10^{13}	0.150		[31]
	Hydrogen abstraction from five-member rings				
4	$C_sR_5{-}H + H \rightarrow C_sR_5^{\bullet} + H_2$	4.890×10^{09}	1.508	19.862	[35]
-4	$C_sR_5^{\bullet} + H_2 \rightarrow C_sR_5 + H$	5.068×10^{04}	2.445	4.520	[35]
5	$C_sR_5{-}H + OH \rightarrow C_sR_5^{\bullet} + H_2O$	5.190×10^{03}	3.040	3.675	[45]
-5	$C_s^{\bullet} + H_2O \rightarrow C_s + OH$	5.590×10^{00}	3.573	8.659	[45]
6	$C_sR_5^{\bullet} + H \rightarrow C_sR_5{-}H$	6.080×10^{12}	0.270		[102]
	Hydrogen addition to five-member rings				
7	$C_sR_5H{-}C_sR_5H + H \rightarrow C_sR_5H_2{-}C_sR_5H^{\bullet}$	5.400×10^{11}	0.450	1.820	[102]
-7	$C_sR_5H_2{-}C_sR_5H^{\bullet} \rightarrow C_sR_5H{-}C_sR_5H + H$	3.015×10^{11}	0.450	−33.367	[102]
8	$C_sR_5H_2{-}C_sR_5H^{\bullet} + H \rightarrow C_sR_5H{-}C_sR_5H + H_2$	2.000×10^{12}			[102]
	Armchair growth				
9	$C_sR_6^{\bullet} + C_2H_2 \rightarrow C_sR_6{-}R_6 + H$	1.190×10^{22}	−2.450	18.890	[26]
10	$C_sR_6^{\bullet} + C_2H_2 \rightarrow C_sR_6{-}R_6 + H$	1.060×10^{14}	−0.490	8.204	[26]
11	$C_sR_6^{\bullet} + C_2H_2 \rightarrow C_sR_6{-}C_2H + H$	4.240×10^{14}	0.025	33.080	[26]
12	$C_sR_6^{\bullet} + C_2H_2 \rightarrow C_sR_6{-}C_2H + H$	7.640×10^{-2}	3.950	16.495	[26]
	Free-edge desorption to produce an armchair				
-9	$C_sR_6{-}R_6 + H \rightarrow C_sR_6^{\bullet} + C_2H_2$	5.465×10^{30}	−3.657	86.240	[26, 63]
-10	$C_sR_6{-}R_6 + H \rightarrow C_sR_6^{\bullet} + C_2H_2$	4.868×10^{22}	−1.697	75.550	[26, 63]
	Free-edge ring growth and desorption				
13	$C_sR_6^{\bullet} + C_2H_2 \rightarrow C_sR_6{-}C_2H_2$	1.910×10^{61}	−14.600	28.610	[56]
-13	$C_sR_6{-}C_2H_2 \rightarrow C_sR_6^{\bullet} + C_2H_2$	2.499×10^{69}	−16.430	71.290	[56]
14	$C_sR_6^{\bullet} + C_2H_2 \rightarrow C_sR_6{-}C_2H + H$	1.100×10^{31}	−4.830	26.620	[56]
-14	$C_sR_6{-}C_2H + H \rightarrow C_sR_6^{\bullet} + C_2H_2$	2.542×10^{37}	−6.213	37.610	[56]
15	$C_sR_6^{\bullet} + C_2H_2 \rightarrow C_sR_6{-}C_2H_3^{\bullet}$	1.360×10^{75}	−18.400	40.880	[56]
-15	$C_sR_6{-}C_2H_3^{\bullet} \rightarrow C_sR_6^{\bullet} + C_2H_2$	4.055×10^{82}	−20.120	79.400	[56]
16	$C_sR_6^{\bullet} + C_2H_3 \rightarrow C_sR_6{-}C_2H_3$	6.000×10^{12}			[63]
-16	$C_sR_6{-}C_2H_3 \rightarrow C_sR_6^{\bullet} + C_2H_2$	8.216×10^{23}	−2.162	119.100	[63]
17	$C_sR_6^{\bullet} + C_2H_4 \rightarrow C_sR_6 + C_2H_3$	9.450×10^{-3}	4.470	4.472	[63]
-17	$C_sR_6 + C_2H_3 \rightarrow C_sR_6^{\bullet} + C_2H_4$	2.316×10^{-2}	4.416	6.709	[63]
18	$C_sR_6^{\bullet} + C_4H_4 \rightarrow C_sR_6{-}R_6 + H$	1.260×10^{04}	2.610	1.434	[63]
-18	$C_sR_6{-}R_6 + H \rightarrow C_sR_6^{\bullet} + C_4H_4$	1.130×10^{16}	0.754	66.940	[63]
19	$C_sR_6 + C_2H_3 \rightarrow C_sR_6{-}C_2H_3 + H$	1.870×10^{07}	1.470	5.533	[63]
-19	$C_sR_6{-}C_2H_3 + H \rightarrow C_sR_6 + C_2H_3$	2.042×10^{14}	−0.221	10.410	[63]
20	$C_sR_6{-}C_2H_3 \rightarrow C_sR_6{-}C_2H_2 + H$	3.010×10^{14}	0.340	111.255	[63]
-20	$C_sR_6{-}C_2H_2 + H \rightarrow C_sR_6{-}C_2H_3$	2.184×10^{11}	0.722		[63]
21	$C_sR_6{-}C_2H_3 + H \rightarrow C_sR_6{-}C_2H_2 + H_2$	6.350×10^{04}	2.750	11.649	[63]
-21	$C_sR_6{-}C_2H_2 + H_2 \rightarrow C_sR_6{-}C_2H_3 + H$	2.509×10^{01}	3.375	3.404	[63]
22	$C_sR_6{-}C_2H_3 + OH \rightarrow C_sR_6{-}C_2H_2 + H_2O$	6.550×10^{-2}	4.200	−0.860	[63]
-22	$C_sR_6{-}C_2H_2 + H_2O \rightarrow C_sR_6{-}C_2H_3 + OH$	6.705×10^{-4}	4.613	6.162	[63]
23	$C_sR_6{-}C_2H_2 \rightarrow C_sR_6{-}C_2H_3^{\bullet}$	2.440×10^{30}	−5.730	32.070	[56]
-23	$C_sR_6{-}C_2H_3^{\bullet} \rightarrow C_sR_6{-}C_2H_2$	5.560×10^{29}	−5.620	27.910	[56]
24	$C_sR_6{-}C_2H_3^{\bullet} + C_2H_2 \rightarrow C_sR_6{-}R_6 + H$	3.020×10^{10}	0.702	5.530	[56]

No.	Reaction	$k = AT^n \exp(-E/RT)$[a]			References
		A	n	E	
-24	$C_sR_6{-}R_6 + H \rightarrow C_sR_6{-}C_2H_3^{\bullet} + C_2H_2$	1.387×10^{21}	-0.798	72.450	[56]
25	$C_sR_6{-}C_2H + H \rightarrow C_sR_6{-}C_2H_2$	1.590×10^{62}	-14.500	31.760	[56]
-25	$C_sR_6{-}C_2H_2 \rightarrow C_sR_6{-}C_2H + H$	9.003×10^{63}	-14.950	63.440	[56]
26	$C_sR_6{-}C_2H_2 + H \rightarrow C_sR_6{-}C_2H + H_2$	1.650×10^{11}	0.490	10.630	[63]
-26	$C_sR_6{-}C_2H + H_2 \rightarrow C_sR_6{-}C_2H_2 + H$	1.587×10^{09}	1.184	82.650	[63]
27	$C_sR_6{-}C_2H_2 + OH \rightarrow C_sR_6{-}C_2H + H_2O$	2.500×10^{12}			[63]
-27	$C_sR_6{-}C_2H + H_2O \rightarrow C_sR_6{-}C_2H_2 + OH$	6.230×10^{11}	0.482	87.280	[63]
28	$C_sR_6{-}C_2H + C_2H_3 \rightarrow C_sR_6{-}R_6 + H$	3.600×10^{17}	-1.440	15.758	[63]
-28	$C_sR_6{-}R_6 + H \rightarrow C_sR_6{-}C_2H + C_2H_3$	1.619×10^{29}	-3.226	74.700	[63]
29	$C_sR_6{-}C_2H^{\bullet} + C_2H_2 \rightarrow C_sR_6{-}R_6^{\bullet}$	4.490×10^{82}	-20.000	51.830	[56]
-29	$C_sR_6{-}R_6^{\bullet} \rightarrow C_sR_6{-}C_2H^{\bullet} + C_2H_2$	1.338×10^{94}	-21.840	143.500	[56]
30	$C_sR_6{-}C_2H^{\bullet} + C_2H_2 \rightarrow C_sR_6{-}R_6^{\bullet}$	1.180×10^{104}	-25.700	76.820	[56]
-30	$C_sR_6{-}R_6^{\bullet} \rightarrow C_sR_6{-}C_2H^{\bullet} + C_2H_2$	3.917×10^{115}	-27.550	168.800	[56]
31	$C_sR_6{-}C_2H^{\bullet} + C_2H_2 \rightarrow C_sR_6{-}R_6^{\bullet}$	4.490×10^{82}	-20.000	51.830	[56]
-31	$C_sR_6{-}R_6^{\bullet} \rightarrow C_sR_6{-}C_2H^{\bullet} + C_2H_2$	1.338×10^{94}	-21.840	143.500	[56]
32	$C_sR_6{-}C_2H^{\bullet} + C_2H_2 \rightarrow C_sR_6(C_2H)(C_2H_3) + H$	1.760×10^{40}	-7.040	48.210	[56]
-32	$C_sR_6(C_2H)(C_2H_3) + H \rightarrow C_sR_6{-}C_2H^{\bullet} + C_2H_2$	9.718×10^{46}	-8.438	60.840	[56]
33	$C_sR_6{-}C_2H^{\bullet} + C_2H_4 \rightarrow C_sR_6{-}R_6 + H$	3.620×10^{28}	-4.240	23.860	[63]
-33	$C_sR_6{-}R_6 + H \rightarrow C_sR_6{-}C_2H^{\bullet} + C_2H_4$	1.583×10^{40}	-6.094	87.580	[63]
34	$C_sR_6{-}C_2H_2 + C_2H_2 \rightarrow C_sR_6{-}R_6 + H$	3.570×10^{22}	-2.720	14.470	[56]
-34	$C_sR_6{-}R_6 + H \rightarrow C_sR_6{-}C_2H_2 + C_2H_2$	3.736×10^{32}	-4.109	77.230	[56]
35	$C_sR_6(C_2H)(C_2H_3) + H \rightarrow C_sR_6{-}R_6^{\bullet}$	1.010×10^{86}	-20.600	56.700	[56]
-35	$C_sR_6{-}R_6^{\bullet} \rightarrow C_sR_6(C_2H)(C_2H_3) + H$	5.450×10^{90}	-21.040	138.800	[56]
36	$C_sR_6(C_2H)(C_2H_3) + H \rightarrow C_sR_6{-}R_6^{\bullet}$	6.000×10^{108}	-26.600	83.590	[56]
-36	$C_sR_6{-}R_6^{\bullet} \rightarrow C_sR_6(C_2H)(C_2H_3) + H$	3.607×10^{113}	-27.050	162.900	[56]
	Six-member bay closure				
37	$C_sR_6{-}H + H \rightarrow C_sR_6^{\bullet} + H_2$	9.240×10^{07}	1.500	9.646	[76]
-37	$C_sR_6^{\bullet} + H_2 \rightarrow C_sR_6 + H$	9.600×10^{04}	1.960	9.021	[76]
38	$C_sR_6^{\bullet} \rightarrow C_sR_6{-}R_6^{\bullet}$	1.110×10^{11}	0.658	23.990	[76]
39	$C_sR_6^{\bullet} \rightarrow C_sR_6{-}R_6^{\bullet}$	3.490×10^{12}	-0.390	2.440	[76]
	Five-member bay closure				
40	$C_sR_6{-}H + H \rightarrow C_sR_6^{\bullet} + H_2$	7.250×10^{07}	1.760	9.69	[91]
-40	$C_sR_6^{\bullet} + H_2 \rightarrow C_sR_6 + H$	3.400×10^{09}	0.880	7.870	[91]
41	$C_sR_6^{\bullet} + C_sR_6{-}H \rightarrow C_sR_6^{\bullet}{-}C_sR_6{-}H$	3.860×10^{11}	0.210	17.700	[91]
	Phenyl addition				
42	$C_sR_6^{\bullet} + A_1 \rightarrow C_sR_6{-}A_1 + H$	2.220×10^{83}	-20.790	46.890	[78]
43	$C_sR_6 + A_1^{\bullet} \rightarrow C_sR_6{-}A_1 + H$	2.220×10^{83}	-20.790	46.890	[78]
	Five-member ring growth on a zig-zag				
44	$C_sR_6^{\bullet} + C_2H_2 \rightarrow C_sR_6{-}R_5 + H$	1.250×10^{27}	-3.950	16.779	[26]
45	$C_sR_6^{\bullet} + C_2H_2 \rightarrow C_sR_6{-}R_5 + H$	3.090×10^{20}	-2.780	8.889	[26]
46	$C_sR_6^{\bullet} + C_2H_2 \rightarrow C_sR_6{-}C_2H + H$	3.090×10^{25}	-3.110	31.586	[26]
47	$C_sR_6^{\bullet} + C_2H_2 \rightarrow C_sR_6{-}C_2H + H$	2.850×10^{7}	1.520	13.190	[26]
	Five-member ring desorption				
48	$C_sR_5^{\bullet} \rightarrow C_sR_6{-}C_2H^{\bullet}$	1.600×10^{14}		42.42	[24]
49	$C_sR_5H_2{-}C_sR_5H^{\bullet} \rightarrow C_sR_6^{\bullet} + C_2H_2$	3.100×10^{11}	0.870	74.323	[102]
50	$C_sR_5H_2{-}C_sR_5H^{\bullet} \rightarrow C_sR_6{-}C_2H + H$	6.700×10^{11}	0.840	70.790	[102]
	Five-member ring migration to a zig-zag site				
51	$C_sR_5H_2{-}C_sR_5H^{\bullet} \rightarrow C_sR_5H^{\bullet}{-}C_sR_5H_2$	1.300×10^{11}	0.160	45.900	[102]
	Five-member ring migration to an armchair site				
52	$C_sR_5H_2{-}C_sR_5H^{\bullet} \rightarrow C_sR_6{-}C_sR_6 + H$	1.300×10^{11}	0.160	45.900	[102]

No.	Reaction	$k = AT^n \exp(-E/RT)$[a]			References
		A	n	E	
	Partially-embedded five-member ring flip reaction				
53	$C_sR_5H^\bullet - CsR_6 \rightarrow CsR_6 - C_sR_5H^\bullet$	1.000×10^{11}			[102, 103]
	Five-member ring conversion to six-member ring neighbouring a free-edge site				
54	$C_sR_6^\bullet + C_2H_2 \rightarrow C_sR_6 - C_2H_2$	1.100×10^{07}	1.610	3.896	[9]
55	$C_sR_6^\bullet + C_2H_2 \rightarrow C_sR_6 - C_2H_2$	3.330×10^{33}	−5.7	25.500	[9, 95]
56	$C_sR_5H_2 - C_sR_5H^\bullet + C_s - C_2H \rightarrow C_sR_6$	1.300×10^{11}	0.160	45.900	[102]
	Six-member ring conversion to five-member ring neighbouring an armchair site				
57	$C_sR_6^\bullet \rightarrow C_sR_5H_2 - C_sR_5H^\bullet + C_s - C_2H$	1.300×10^{11}	1.080	70.420	[24]
	Six-member ring conversion to five-member ring neighbouring a five-carbon bay site				
58	$C_{s-BY5} - C_sR_6^\bullet \rightarrow CsR_6 - C_sR_5 - C_sR_5 + H$	2.300×10^{09}	1.603	61.850	[76]
59	$C_{s-BY5} - C_sR_6^\bullet \rightarrow CsR_6 - C_sR_5 - C_sR_5 + H$	1.230×10^{10}	1.410	85.200	[91]
	Six-member ring desorption neighbouring a five-carbon bay site				
60	$C_{s-BY5} - C_sR_6^\bullet \rightarrow CsR_6 - C_sR_6^\bullet + C_2H_2$	2.300×10^{09}	1.603	61.850	[76]
	Migration of partially-embedded five-member ring				
61	$C_sR_5 - C_sR_5 - C_sR_6^\bullet \rightarrow CsR_6^\bullet - C_sR_5 - C_sR_5H$	5.188×10^{13}		33.400	[104]
62	$C_sR_5H - C_sR_5 - C_sR_6^\bullet \rightarrow CsR_6^\bullet - C_sR_5 - C_sR_5$	1.037×10^{14}		33.400	[104]
	Six-member ring growth on a zig-zag neighbouring a five-member ring				
63	$C_sR_5^\bullet + C_2H_2 \rightarrow CsR_5 - R_6$	1.235×10^{07}	1.530	9.311	[102]
	Six-member ring growth between two five-member rings				
64	$C_sR_5^\bullet + C_2H_2 \rightarrow CsR_5 - R_6$	1.235×10^{07}	1.530	9.311	[102]
	Five-member ring conversion to six-member ring neighbouring five-member ring				
65	$C_sR_5^\bullet + C_sR_5H \rightarrow CsR_6 - R_5$	8.900×10^{05}	2.280	61.489	[102]
	Six-member bay closure containing a partially-embedded five-member ring				
66	$C_sR_6^\bullet \rightarrow C_sR_6 - R_6^\bullet$	1.110×10^{11}	0.658	23.990	[50]
	Six-member ring growth on a partially-embedded five-member ring armchair				
67	$C_sR_6 - H + H \rightarrow C_sR_6^\bullet + H_2$	2.540×10^{11}	0.931	16.440	[75]
-67	$C_sR_6^\bullet + H_2 \rightarrow C_sR_6 + H$	1.830×10^{12}	0.397	8.815	[75]
68	$C_sR_6^\bullet + C_2H_2 \rightarrow C_sR_6 - C_2H_2$	1.630×10^{12}	0.409	5.675	[75]
-68	$C_sR_6 - C_2H_2 \rightarrow C_sR_6^\bullet + C_2H_2$	9.130×10^{11}	0.991	15.990	[75]
69	$C_sR_6 - C_2H_2 \rightarrow C_sR_6^\bullet - C_2H_3$	6.320×10^{11}	0.166	18.050	[75]
-69	$C_sR_6^\bullet - C_2H_3 \rightarrow C_sR_6 - C_2H_2$	9.750×10^{10}	0.458	15.830	[75]
70	$C_sR_6^\bullet - C_2H_3 \rightarrow C_sR_6H_2 - CsR_6H^\bullet$	9.580×10^{11}	−0.064	16.310	[75]
-70	$C_sR_6H_2 - CsR_6H^\bullet \rightarrow C_sR_6^\bullet - C_2H_3$	9.650×10^{11}	0.501	41.500	[75]
71	$C_sR_6H_2 - CsR_6H^\bullet \rightarrow C_sR_6 - CsR_6 + H$	3.160×10^{12}	0.787	36.510	[75]
-71	$C_sR_6 - CsR_6 + H \rightarrow C_sR_6H_2 - CsR_6H^\bullet$	9.710×10^{11}	0.507	4.695	[75]
72	$C_sR_6^\bullet - C_2H_3 \rightarrow C_sR_6H - CsR_6$	2.780×10^{11}	0.063	23.870	[75]
-72	$C_sR_6H - CsR_6 \rightarrow C_sR_6^\bullet - C_2H_3$	5.470×10^{11}	0.645	32.770	[75]
73	$C_sR_6H - CsR_6 \rightarrow C_sR_6 - CsR_6 + H$	8.150×10^{11}	0.563	24.860	[75]
-73	$C_sR_6 - CsR_6 + H \rightarrow C_sR_6H - CsR_6$	9.060×10^{11}	0.456	7.286	[75]
	Seven-member ring growth on a five-carbon bay site (partially-embedded five-member ring)				
74	$C_sR_6 - H + H \rightarrow C_sR_6^\bullet + H_2$	5.897×10^{07}	1.847	17.120	[57]
-74	$C_sR_6^\bullet + H_2 \rightarrow C_sR_6 + H$	1.215×10^{05}	2.229	7.720	[57]
75	$C_sR_6^\bullet + C_2H_2 \rightarrow C_sR_6 - C_2H_2$	1.348×10^{03}	2.573	4.935	[57]
-75	$C_sR_6 - C_2H_2 \rightarrow C_sR_6^\bullet + C_2H_2$	2.366×10^{12}	0.705	39.670	[57]
76	$C_sR_6 - C_2H_2 \rightarrow C_sR_6H - C_sR_6^\bullet$	1.958×10^{11}	0.111	25.330	[57]
-76	$C_sR_6H - C_sR_6^\bullet \rightarrow C_sR_6 - C_2H_2$	3.412×10^{11}	0.625	53.370	[57]
77	$C_sR_6H - C_sR_6^\bullet \rightarrow C_sR_6 - CsR_6 + H$	1.770×10^{10}	1.094	27.150	[57]
-77	$C_sR_6 - CsR_6 + H \rightarrow C_sR_6H - C_sR_6^\bullet$	5.321×10^{07}	1.515	7.095	[57]
78	$C_sR_6 - H + H \rightarrow C_sR_6^\bullet + H_2$	5.315×10^{07}	1.858	16.120	[57]
-78	$C_sR_6^\bullet + H_2 \rightarrow C_sR_6 + H$	9.106×10^{04}	2.277	7.007	[57]

No.	Reaction	$k = AT^n \exp(-E/RT)$[a]			References
		A	n	E	
79	$C_sR_6^\bullet + C_2H_2 \rightarrow C_sR_6{-}C_2H_2$	3.521×10^{03}	2.598	3.998	[57]
-79	$C_sR_6{-}C_2H_2 \rightarrow C_sR_6^\bullet + C_2H_2$	4.736×10^{12}	0.702	40.800	[57]
80	$C_sR_6{-}C_2H_2 \rightarrow C_sR_6H{-}C_sR_6^\bullet$	1.125×10^{11}	0.128	30.510	[57]
-80	$C_sR_6H{-}C_sR_6^\bullet \rightarrow C_sR_6{-}C_2H_2$	2.383×10^{11}	0.596	57.900	[57]
81	$C_sR_6H{-}C_sR_6^\bullet \rightarrow C_sR_6{-}CsR_6 + H$	1.505×10^{10}	1.076	28.840	[57]
-81	$C_sR_6{-}CsR_6 + H \rightarrow C_sR_6H{-}C_sR_6^\bullet$	5.841×10^{07}	1.533	7.084	[57]
	Seven-member ring growth on a five-carbon bay site (edge five-member ring)				
82	$C_sR_6{-}H + H \rightarrow C_sR_6^\bullet + H_2$	6.586×10^{07}	1.766	14.770	[57]
-82	$C_sR_6^\bullet + H_2 \rightarrow C_sR_6 + H$	1.155×10^{05}	2.310	8.819	[57]
83	$C_sR_6^\bullet + C_2H_2 \rightarrow C_sR_6{-}C_2H_2$	3.886×10^{03}	2.592	4.012	[57]
-83	$C_sR_6{-}C_2H_2 \rightarrow C_sR_6^\bullet + C_2H_2$	6.507×10^{12}	0.710	45.050	[57]
84	$C_sR_6{-}C_2H_2 \rightarrow C_sR_6H{-}C_sR_6^\bullet$	5.755×10^{11}	0.070	2.983	[57]
-84	$C_sR_6H{-}C_sR_6^\bullet \rightarrow C_sR_6{-}C_2H_2$	1.742×10^{12}	0.419	29.040	[57]
85	$C_sR_6H{-}C_sR_6^\bullet \rightarrow C_sR_6{-}CsR_6 + H$	3.207×10^{10}	0.958	23.130	[57]
-85	$C_sR_6{-}CsR_6 + H \rightarrow C_sR_6H{-}C_sR_6^\bullet$	1.293×10^{08}	1.505	7.425	[57]
86	$C_sR_5{-}H + H \rightarrow C_sR_5^\bullet + H_2$	1.479×10^{07}	1.854	17.070	[57]
-86	$C_sR_5^\bullet + H_2 \rightarrow C_sR_5 + H$	5.914×10^{04}	2.234	11.870	[57]
87	$C_sR_5^\bullet + C_2H_2 \rightarrow C_sR_5{-}C_2H_2$	1.098×10^{03}	2.581	7.651	[57]
-87	$C_sR_5{-}C_2H_2 \rightarrow C_sR_5^\bullet + C_2H_2$	2.894×10^{12}	0.709	38.300	[57]
88	$C_sR_5{-}C_2H_2 \rightarrow C_sR_5H{-}C_sR_6^\bullet$	5.097×10^{11}	0.139	19.740	[57]
-88	$C_sR_5H{-}C_sR_6^\bullet \rightarrow C_sR_5{-}C_2H_2$	9.936×10^{11}	0.410	45.260	[57]
89	$C_sR_5H{-}C_sR_6^\bullet \rightarrow C_sR_5{-}CsR_6 + H$	3.590×10^{11}	0.604	30.050	[57]
-89	$C_sR_5{-}CsR_6 + H \rightarrow C_sR_5H{-}C_sR_6^\bullet$	6.258×10^{08}	1.380	24.510	[57]
	Seven-member bay closure (H abstraction on site 1)				
90	$C_sR_6{-}H + H \rightarrow C_sR_6^\bullet + H_2$	3.915×10^{07}	1.876	9.421	[57]
-90	$C_sR_6^\bullet + H_2 \rightarrow C_sR_6 + H$	5.369×10^{04}	2.275	5.583	[57]
91	$C_sR_6^\bullet + C_sR_6{-}H \rightarrow C_sR_7{-}C_sR_7{-}H$	8.513×10^{11}	0.136	4.510	[57]
-91	$C_sR_7{-}C_sR_7{-}H \rightarrow C_sR_6^\bullet + C_sR_6{-}H$	3.523×10^{12}	0.293	25.670	[57]
92	$C_sR_7{-}C_sR_7{-}H \rightarrow C_sR_7{-}C_sR_7 + H$	2.033×10^{10}	1.067	31.600	[57]
-92	$C_sR_7{-}C_sR_7 + H \rightarrow C_sR_7{-}C_sR_7{-}H$	1.033×10^{08}	1.495	2.895	[57]
93	$C_sR_6{-}H + H \rightarrow C_sR_6^\bullet + H_2$	3.091×10^{07}	1.891	9.308	[57]
-93	$C_sR_6^\bullet + H_2 \rightarrow C_sR_6 + H$	5.144×10^{04}	2.267	7.132	[57]
94	$C_sR_6^\bullet + C_sR_6{-}H \rightarrow C_sR_7{-}C_sR_7{-}H$	7.041×10^{11}	0.184	10.340	[57]
-94	$C_sR_7{-}C_sR_7{-}H \rightarrow C_sR_6^\bullet + C_sR_6{-}H$	2.944×10^{12}	0.413	28.620	[57]
95	$C_sR_7{-}C_sR_7{-}H \rightarrow C_sR_7{-}C_sR_7 + H$	1.861×10^{10}	1.136	29.570	[57]
-95	$C_sR_7{-}C_sR_7 + H \rightarrow C_sR_7{-}C_sR_7{-}H$	7.712×10^{07}	1.514	2.067	[57]
	Seven-member bay closure (Carbene route on site 1)				
96	$C_sR_6{-}H + C_sR_6{-}H \rightarrow C_sR_6^{(2\bullet)} + C_sR_6{-}H_2$	8.031×10^{10}	0.890	95.830	[57]
-96	$C_sR_6^{(2\bullet)} + C_sR_6{-}H_2 \rightarrow C_sR_6{-}H + C_sR_6{-}H$	4.398×10^{11}	0.359	3.385	[57]
97	$C_sR_6^{(2\bullet)} + C_sR_6{-}H \rightarrow C_sR_7{-}C_sR_7{-}H$	8.031×10^{11}	0.010	8.456	[57]
-97	$C_sR_7{-}C_sR_7{-}H \rightarrow C_sR_6^{(2\bullet)} + C_sR_6{-}H$	1.897×10^{12}	0.223	17.790	[57]
98	$C_sR_7{-}H + C_sR_7 \rightarrow C_sR_7 + C_sR_7{-}H$	5.759×10^{11}	0.393		[57]
-98	$C_sR_7 + C_sR_7{-}H \rightarrow C_sR_7{-}H + C_sR_7$	1.052×10^{11}	0.905	53.500	[57]
99	$C_sR_7{-}H + C_sR_6{-}H \rightarrow C_sR_7 + C_sR_6{-}H_2 + H_2$	8.873×10^{10}	0.639	31.310	[57]
-99	$C_sR_7 + C_sR_6{-}H_2 \rightarrow C_sR_7{-}H + C_sR_6{-}H$	1.728×10^{10}	0.712	60.650	[57]
100	$C_sR_6{-}H_2 + C_sR_6{-}H_2 \rightarrow C_sR_6{-}H + C_sR_6{-}H + H_2$	3.907×10^{09}	1.273	97.050	[57]
-100	$C_sR_6{-}H + C_sR_6{-}H + H_2 \rightarrow C_sR_6{-}H_2 + C_sR_6{-}H_2$	2.448×10^{05}	1.999	86.400	[57]
101	$C_sR_6{-}H + C_sR_6{-}H \rightarrow C_sR_6^{(2\bullet)} + C_sR_6{-}H_2$	1.061×10^{11}	0.799	84.260	[57]
-101	$C_sR_6^{(2\bullet)} + C_sR_6{-}H_2 \rightarrow C_sR_6{-}H + C_sR_6{-}H$	5.486×10^{11}	0.335	2.012	[57]

No.	Reaction	$k = AT^n \exp(-E/RT)$[a]			References
		A	n	E	
102	$C_sR_6^{(2\bullet)} + C_sR_6{-}H \rightarrow C_sR_7{-}C_sR_7{-}H$	1.000×10^{12}	-0.014	3.568	[57]
-102	$C_sR_7{-}C_sR_7{-}H \rightarrow C_sR_6^{(2\bullet)} + C_sR_6{-}H$	2.167×10^{12}	0.556	59.280	[57]
103	$C_sR_7{-}H + C_sR_6{-}H \rightarrow C_sR_7 + C_sR_6{-}H_2$	3.063×10^{11}	0.824	63.560	[57]
-103	$C_sR_7 + C_sR_6{-}H_2 \rightarrow C_sR_7{-}H + C_sR_6{-}H$	1.514×10^{10}	0.674	50.310	[57]
104	$C_sR_6{-}H_2 + C_sR_6{-}H_2 \rightarrow C_sR_6{-}H + C_sR_6{-}H + H_2$	4.479×10^{09}	0.714	27.100	[57]
-104	$C_sR_6{-}H + C_sR_6{-}H + H_2 \rightarrow C_sR_6{-}H_2 + C_sR_6{-}H_2$	2.332×10^{05}	1.742	55.100	[57]
	Seven-member bay closure (H abstraction on site 2)				
105	$C_sR_6{-}H + H \rightarrow C_sR_6^{\bullet} + H_2$	2.767×10^{07}	1.913	9.542	[57]
-105	$C_sR_6^{\bullet} + H_2 \rightarrow C_sR_6 + H$	4.212×10^{04}	2.264	6.878	[57]
106	$C_sR_6^{\bullet} + C_sR_6{-}H \rightarrow C_sR_7{-}C_sR_7{-}H$	4.703×10^{11}	0.143	4.722	[57]
-106	$C_sR_7{-}C_sR_7{-}H \rightarrow C_sR_6^{\bullet} + C_sR_6{-}H$	1.476×10^{12}	0.367	27.37	[57]
107	$C_sR_7{-}C_sR_7{-}H \rightarrow C_sR_7{-}C_sR_7 + H$	6.424×10^{09}	1.093	32.16	[57]
-107	$C_sR_7{-}C_sR_7 + H \rightarrow C_sR_7{-}C_sR_7{-}H$	1.693×10^{08}	1.522	1.637	[57]
108	$C_sR_6{-}H + H \rightarrow C_sR_6^{\bullet} + H_2$	2.843×10^{07}	1.906	9.533	[57]
-108	$C_sR_6^{\bullet} + H_2 \rightarrow C_sR_6 + H$	5.338×10^{04}	2.261	7.525	[57]
109	$C_sR_6^{\bullet} + C_sR_6{-}H \rightarrow C_sR_7{-}C_sR_7{-}H$	6.599×10^{11}	0.082	2.625	[57]
-109	$C_sR_7{-}C_sR_7{-}H \rightarrow C_sR_6^{\bullet} + C_sR_6{-}H$	5.132×10^{12}	0.340	25.40	[57]
110	$C_sR_7{-}C_sR_7{-}H \rightarrow C_sR_7{-}C_sR_7 + H$	2.006×10^{10}	1.099	32.81	[57]
-110	$C_sR_7{-}C_sR_7 + H \rightarrow C_sR_7{-}C_sR_7{-}H$	1.729×10^{08}	1.489	1.504	[57]
	Seven-member bay closure (Carbene route on site 2)				
111	$C_sR_6{-}H + C_sR_6{-}H \rightarrow C_sR_6^{(2\bullet)} + C_sR_6{-}H_2$	1.603×10^{11}	0.777	83.23	[57]
-111	$C_sR_6^{(2\bullet)} + C_sR_6{-}H_2 \rightarrow C_sR_6{-}H + C_sR_6{-}H$	3.050×10^{11}	0.294		[57]
112	$C_sR_6^{(2\bullet)} + C_sR_6{-}H \rightarrow C_sR_7{-}C_sR_7{-}H$	2.488×10^{11}	0.120	11.62	[57]
-112	$C_sR_7{-}C_sR_7{-}H \rightarrow C_sR_6^{(2\bullet)} + C_sR_6{-}H$	1.472×10^{12}	0.676	45.09	[57]
113	$C_sR_7{-}H + C_sR_7 \rightarrow C_sR_7 + C_sR_7{-}H$	1.397×10^{11}	0.581	27.01	[57]
-113	$C_sR_7 + C_sR_7{-}H \rightarrow C_sR_7{-}H + C_sR_7$	3.264×10^{10}	0.734	56.81	[57]
114	$C_sR_7{-}H + C_sR_6{-}H \rightarrow C_sR_7 + C_sR_6{-}H_2 + H_2$	5.515×10^{10}	0.849	59.32	[57]
-114	$C_sR_7 + C_sR_6{-}H_2 \rightarrow C_sR_7{-}H + C_sR_6{-}H$	7.566×10^{10}	0.675	38.56	[57]
115	$C_sR_6{-}H_2 + C_sR_6{-}H_2 \rightarrow C_sR_6{-}H + C_sR_6{-}H + H_2$	6.206×10^{09}	0.848	28.61	[57]
-115	$C_sR_6{-}H + C_sR_6{-}H + H_2 \rightarrow C_sR_6{-}H_2 + C_sR_6{-}H_2$	2.164×10^{05}	1.798	58.70	[57]
116	$C_sR_6{-}H + C_sR_6{-}H \rightarrow C_sR_6^{(2\bullet)} + C_sR_6{-}H_2$	1.162×10^{11}	0.837	86.01	[57]
-116	$C_sR_6^{(2\bullet)} + C_sR_6{-}H_2 \rightarrow C_sR_6{-}H + C_sR_6{-}H$	4.948×10^{11}	0.331	1.476	[57]
117	$C_sR_6^{(2\bullet)} + C_sR_6{-}H \rightarrow C_sR_7{-}C_sR_7{-}H$	5.744×10^{11}	0.039	8.721	[57]
-117	$C_sR_7{-}C_sR_7{-}H \rightarrow C_sR_6^{(2\bullet)} + C_sR_6{-}H$	2.164×10^{12}	0.292	18.61	[57]
118	$C_sR_7{-}H + C_sR_6{-}H \rightarrow C_sR_7 + C_sR_6{-}H_2$	9.900×10^{11}	0.331	-2.850	[57]
-118	$C_sR_7 + C_sR_6{-}H_2 \rightarrow C_sR_7{-}H + C_sR_6{-}H$	1.025×10^{11}	0.875	57.11	[57]
119	$C_sR_7{-}H + C_sR_6{-}H \rightarrow C_sR_7 + C_sR_6{-}H_2 + H_2$	6.156×10^{10}	0.782	39.25	[57]
-119	$C_sR_7 + C_sR_6{-}H_2 \rightarrow C_sR_7{-}H + C_sR_6{-}H$	9.567×10^{10}	0.696	35.20	[57]
120	$C_sR_6{-}H_2 + C_sR_6{-}H_2 \rightarrow C_sR_6{-}H + C_sR_6{-}H + H_2$	3.478×10^{09}	1.288	87.43	[57]
-120	$C_sR_6{-}H + C_sR_6{-}H + H_2 \rightarrow C_sR_6{-}H_2 + C_sR_6{-}H_2$	1.696×10^{05}	2.086	95.63	[57]
	Methyl addition				
121	$C_sR_6^{\bullet} + CH_3 \rightarrow C_sR_6{-}CH_3$	2.331×10^{14}	-0.283	-0.191	[46]
	Methyl desorption				
122	$C_sR_6{-}CH_3 \rightarrow C_sR_6^{\bullet} + CH_3$	1.950×10^{27}	-3.160	107.447	[46]
123[b]	$C_sR_6{-}CH_3 \rightarrow C_sR_6^{\bullet} + CH_3$	7.055×10^{-1}	-22.966	122.080	[46]
	Six-member ring oxidation				
124	$C_sR_6^{\bullet} + O_2 \rightarrow C_sR_6{-}O^{\bullet} + O$	3.170×10^{13}		2.021	[85]
125	$C_sR_{6i}{-}O^{\bullet} \rightarrow C_sR_5 + CO$	1.760×10^{23}	-3.681	48.000	[52]
126	$C_sR_{6j}{-}O^{\bullet} \rightarrow C_sR_5 + CO$	8.820×10^{09}	-0.063	33.010	[52]

No.	Reaction	$k = AT^n \exp(-E/RT)$[a]			References
		A	n	E	
127	$C_sR_6^\bullet + OH \rightarrow C_sR_5 + CO$	1.000×10^{14}			[25]
128	$C_sR_6^\bullet + OH \rightarrow C_sR_6{-}OH$	1.470×10^{14}		1.256	[85]
-128	$C_sR_6{-}OH \rightarrow C_sR_6^\bullet + OH$	2.140×10^{16}		105.292	[85]
129	$C_sR_6{-}OH \rightarrow C_sR_6{-}O^\bullet + H$	2.130×10^{15}		84.064	[85]
-129	$C_sR_6{-}O^\bullet + H \rightarrow C_sR_6{-}OH$	4.340×10^{14}		1.955	[85]
130	$C_sR_6{-}OH + H \rightarrow C_sR_6{-}O^\bullet + H_2$	5.477×10^{06}	2.147	11.134	[85]
-130	$C_sR_6{-}O^\bullet + H_2 \rightarrow C_sR_6{-}OH + H$	1.700×10^{14}		19.146	[85]
131	$C_sR_6{-}OH + H \rightarrow C_sR_6^\bullet + H_2O$	2.000×10^{14}		5.306	[85]
132	$C_sR_6H + O \rightarrow C_sR_6{-}O^\bullet + H$	4.000×10^{12}		4.626	[25]
	Partially-embedded five-member ring oxidation				
133	$C_sR_6{-}C_sR_5H{-}C_sR_6 + O_2 \rightarrow C_sR_6^\bullet{-}C_sR_6H + CO_2$	3.450×10^{11}		26.670	[25]
134	$C_sR_6{-}C_sR_5H{-}C_sR_6 + O \rightarrow C_sR_6^\bullet{-}C_sR_6H + CO$	3.541×10^{11}	0.505	0.608	[25]
	Five- Seven-member ring recombination				
135	$C_sR_7H{-}C_sR_5 + H \rightarrow C_sR_7H_2{-}C_sR_5$	3.480×10^{08}	1.490	3.440	[57]
-135	$C_sR_7H_2{-}C_sR_5 \rightarrow C_sR_7H{-}C_sR_5 + H$	2.340×10^{09}	1.180	30.770	[57]
136	$C_sR_7H_2{-}C_sR_5 \rightarrow C_sR_7H{-}C_sR_5H$	2.120×10^{10}	0.670	40.320	[57]
-136	$C_sR_7H{-}C_sR_5H \rightarrow C_sR_7H_2{-}C_sR_5$	8.390×10^{11}	0.290	18.610	[57]
137	$C_sR_7H{-}C_sR_5H \rightarrow C_sR_3H{-}C_sR_3H$	1.030×10^{12}	0.150	9.250	[57]
-137	$C_sR_3H{-}C_sR_3H \rightarrow C_sR_7H{-}C_sR_5H$	1.870×10^{12}	0.320	15.040	[57]
138	$C_sR_3H{-}C_sR_3H \rightarrow C_sR_6H{-}C_sR_6H$	6.650×10^{12}	-0.130	4.090	[57]
-138	$C_sR_6H{-}C_sR_6H \rightarrow C_sR_3H{-}C_sR_3H$	1.520×10^{12}		34.080	[57]
139	$C_sR_6H{-}C_sR_6H \rightarrow C_sR_6{-}C_sR_6H + H$	1.130×10^{10}	1.000	15.650	[57]
-139	$C_sR_6{-}C_sR_6H + H \rightarrow C_sR_6H{-}C_sR_6H$	2.820×10^{08}	1.360	35.440	[57]

Notes:
[a] The units are mole, centimetre, second, and kilocalorie.
The reverse rate coefficients were calculated via equilibrium constants.
[b] Low-pressure limit in TROE form.
Parameters $A = 0.70546$, $T_3 = 9.999E+09$ K, $T_1 = 459.918$ K, $T_2 = -8.214E+09$ K.

Table A.2: *Kinetic Monte Carlo jump processes.*

Process	Parent site
S1 Free-edge ring growth [9]	**Free-edge (FE)**
Jump process: 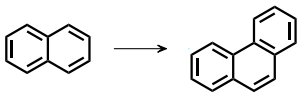	Rate: [a] $\Big(k_{18}[C_sR_6^{\bullet}][C_4H_4]+k_{24}[C_sR_6{-}C_2H_3^{\bullet}][C_2H_2]+k_{28}[C_sR_6{-}C_2H][C_2H_3]+ k_{29}[C_sR_6{-}C_2H^{\bullet}][C_2H_2]+k_{30}[C_sR_6{-}C_2H^{\bullet}][C_2H_2]+k_{31}[C_sR_6{-}C_2H^{\bullet}][C_2H_2]+ k_{33}[C_sR_6{-}C_2H^{\bullet}][C_2H_4]+k_{34}[C_sR_6{-}C_2H_2][C_2H_2]+k_{35}[C_sR_6(C_2H)(C_2H_3)][H]+ k_{36}[C_sR_6(C_2H)(C_2H_3)][H]\Big)[C_{FE}]$
S2 Armchair ring growth [9]	**Armchair (AC)**
Jump process: 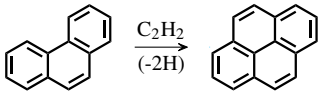	Rate: $(k_9+k_{10})\left(\frac{k_1[H]+k_2[OH]}{k_{-1}[H_2]+k_3[H]+k_{-2}[H_2O]+(k_9+k_{10}+k_{11}+k_{12})[C_2H_2]}\right)[C_2H_2][C_{AC}]$
S3 Free-edge desorption to an armchair [26, 63]	**Free-edge adjacent to non-free-edges (FE_{HACA})**
Jump process: 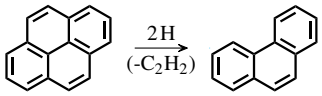	Rate: $(k_{-9}+k_{-10})[C_{FE_{HACA}}]$
S4 Free-edge ring desorption [9]	**Free-edge with two adjacent free-edges (FE3)**
Jump process: 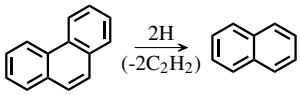	Rate: $\Big(k_{-18}+k_{-24}+k_{-28}+k_{-33}+k_{-34}+k_{-35}\Big)[H][C_{FE3}]+ \left(\frac{(k_1[H]+k_2[OH])(k_{-29}+k_{-30}+k_{-31})}{k_{-1}[H_2]+k_3[H]+k_{-2}[H_2O]}\right)[C_{FE3}]$
S5 6- to 5-member ring conversion at armchair [9]	**Armchair next to FE3 (AC_{FE3})**
Jump process: 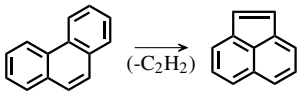	Rate: $k_{57}\left(\frac{k_1[H]+k_2[OH]}{k_{-1}[H_2]+k_3[H]+k_{-2}[H_2O]+k_{57}}\right)[C_{AC_{FE3}}]$
S6 5-member ring addition [9]	**Zig-zag (ZZ)**
Jump process: 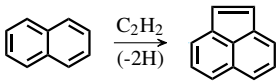	Rate: $(k_{44}+k_{45})\left(\frac{k_1[H]+k_2[OH]}{k_{-1}[H_2]+k_3[H]+k_{-2}[H_2O]+(k_{44}+k_{45}+k_{46}+k_{47})[C_2H_2]}\right)[C_2H_2][C_{ZZ}]$
S7 5-member ring desorption [9]	**5-member ring (R5)**
Jump process: 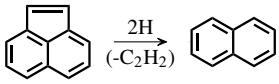	Rate: $\left(\frac{k_{48}(k_4[H]+k_5[OH])}{k_{-4}[H_2]+k_6[H]+k_{-5}[H_2O]+k_{48}}+\frac{k_7[H](k_{49}+k_{50})}{k_{-7}[H]+k_8[H]+k_{49}+k_{50}}\right)[C_{R5}]$

Process	Parent site
S8 5- to 6-member ring conversion at free edge [9]	**5-member ring next to free-edge (RFE)**
Jump process: 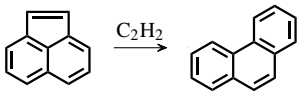	Rate: $(k_{54}+k_{55})\left(\frac{k_7[\mathrm{H}]}{k_{-7}[\mathrm{H}]+k_8[\mathrm{H}]+k_{49}+k_{50}+k_{51}+(k_{54}+k_{55})f[\mathrm{C_2H_2}]}\right) f[\mathrm{C_2H_2}][\mathrm{C_{RFE}}]$, where $f=\left(\frac{k_1[\mathrm{H}]+k_2[\mathrm{OH}]}{k_{-1}[\mathrm{H_2}]+k_3[\mathrm{H}]+k_{-2}[\mathrm{H_2O}]+(k_{54}+k_{55})[\mathrm{C_2H_2}]}\right)$
S9 5- to 6-member ring conversion at armchair [9]	**5-member ring next to armchair (RAC)**
Jump process: 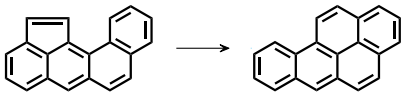	Rate: $k_{52}\left(\frac{k_7[\mathrm{H}]}{k_{-7}[\mathrm{H}]+k_8[\mathrm{H}]+k_{49}+k_{50}+k_{51}+k_{52}}\right)[\mathrm{C_{RAC}}]$
S10 Benzene addition [76]	**All site types**
Jump process: 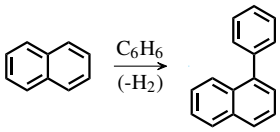	Rate: $2k_{42}\left(\frac{k_1[\mathrm{H}]+k_2[\mathrm{OH}]}{k_{-1}[\mathrm{H_2}]+k_3[\mathrm{H}]+k_{-2}[\mathrm{H_2O}]+k_{42}[\mathrm{C_6H_6}]}\right)[\mathrm{C_6H_6}][\mathrm{C_s}]$
S11 5-member ring migration [76]	**5-member ring next to zig-zag (RZZ)**
Jump process: 	Rate: $k_{51}\left(\frac{k_7[\mathrm{H}]}{k_{-7}[\mathrm{H}]+k_8[\mathrm{H}]+k_{49}+k_{50}+k_{51}}\right)[\mathrm{C_{RZZ}}]$
S12 Ring growth next to 5-member ring [102]	**5-member ring next to zig-zag (RZZ)**
Jump process: 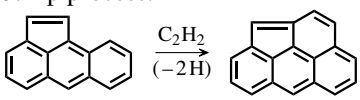	Rate: $k_{63}\left(\frac{k_1[\mathrm{H}]+k_2[\mathrm{OH}]}{k_{-1}[\mathrm{H_2}]+k_3[\mathrm{H}]+k_{-2}[\mathrm{H_2O}]+k_{63}[\mathrm{C_2H_2}]}+\frac{k_4[\mathrm{H}]+k_5[\mathrm{OH}]}{k_{-4}[\mathrm{H_2}]+k_6[\mathrm{H}]+k_{-5}[\mathrm{H_2O}]+k_{63}[\mathrm{C_2H_2}]}\right)[\mathrm{C_{RZZ}}]$
S13 Ring growth between 5-member rings [102]	**Free-edge between 5-member rings (RFER)**
Jump process: 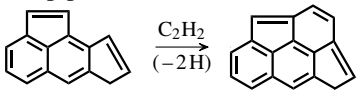	Rate: $k_{64}\left(\frac{k_4[\mathrm{H}]+k_5[\mathrm{OH}]}{k_{-4}[\mathrm{H_2}]+k_6[\mathrm{H}]+k_{-5}[\mathrm{H_2O}]+k_{64}[\mathrm{C_2H_2}]}\right)[\mathrm{C_{RFER}}]$
S14 5-member rings collision [102]	**Zig-zag between 5-member rings (RZZR)**
Jump process: 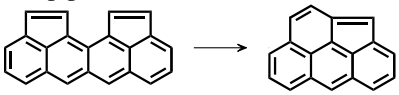	Rate: $2k_{65}\left(\frac{k_7[\mathrm{H}]}{k_{-7}[\mathrm{H}]+k_8[\mathrm{H}]+k_{49}+k_{50}+k_{65}}\right)[\mathrm{C_{RZZR}}]$
S15 6-member bay closure [76]	**6-member bay (BY6)**
Jump process: 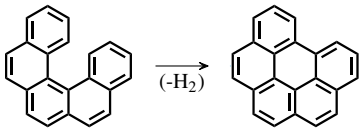	Rate: $2(k_{38}+k_{39})\left(\frac{k_{37}[\mathrm{H}]+k_2[\mathrm{OH}]}{k_{-37}[\mathrm{H_2}]+k_3[\mathrm{H}]+k_{-2}[\mathrm{H_2O}]+k_{38}+k_{39}}\right)[\mathrm{C_{BY6}}]$

Process	Parent site
S16 5-member bay closure [76]	**5-member bay (BY5)**
Jump process: 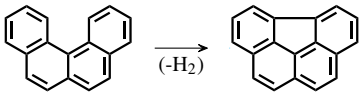 Rate: $2k_{41}\left(\frac{k_{40}[\mathrm{H}]+k_2[\mathrm{OH}]}{k_{-40}[\mathrm{H_2}]+k_3[\mathrm{H}]+k_{-2}[\mathrm{H_2O}]+k_{41}}\right)[\mathrm{C_{BY5}}]$	
S17 6-member bay closure [76] **(partially-embedded 5-member ring)**	**6-member bay ($\mathrm{BY6_{eR5}}$) with partially-embedded 5-member ring**
Jump process: 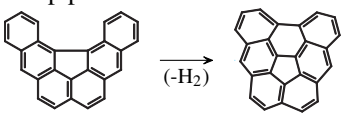 Rate: $2k_{66}\left(\frac{k_{37}[\mathrm{H}]+k_2[\mathrm{OH}]}{k_{-37}[\mathrm{H_2}]+k_3[\mathrm{H}]+k_{-2}[\mathrm{H_2O}]+k_{66}}\right)[\mathrm{C_{BY6_{eR5}}}]$	
S18 Partially-embedded 5-member ring migration [104] **from edge position**	**Partially-embedded 5-member ring (eR5) in edge position**
Jump process: 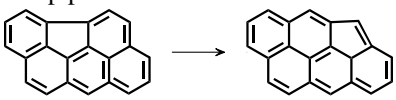 Rate: $k_{61}\left(\frac{k_3[\mathrm{H}]+k_2[\mathrm{OH}]}{k_{-1}[\mathrm{H_2}]+k_3[\mathrm{H}]+k_{-2}[\mathrm{H_2O}]+k_{61}}\right)[\mathrm{C_{eR5}}]$	
S19 Partially-embedded 5-member ring migration [104] **from corner position**	**Partially-embedded 5-member ring (cR5) in corner position**
Jump process: 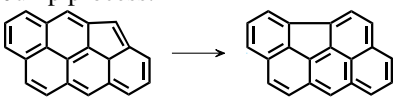 Rate: $k_{62}\left(\frac{k_3[\mathrm{H}]+k_2[\mathrm{OH}]}{k_{-1}[\mathrm{H_2}]+k_3[\mathrm{H}]+k_{-2}[\mathrm{H_2O}]+k_{62}}\right)[\mathrm{C_{cR5}}]$	
S20 6-member ring desorption at bay [77]	**BY5 next to FE3 ($\mathrm{BY5_{FE3}}$)**
Jump process: 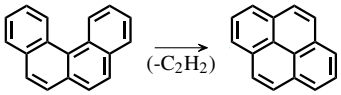 Rate: $k_{60}\left(\frac{k_1[\mathrm{H}]+k_2[\mathrm{OH}]}{k_{-1}[\mathrm{H_2}]+k_3[\mathrm{H}]+k_{-2}[\mathrm{H_2O}]+k_{60}}\right)[\mathrm{C_{BY5_{FE3}}}]$	
S21 6-member ring rearrangement at bay [77]	**BY5 next to FE3 ($\mathrm{BY5_{FE3}}$)**
Jump process: 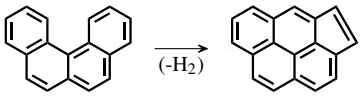 Rate: $(k_{58}+k_{59})\left(\frac{k_1[\mathrm{H}]+k_2[\mathrm{OH}]}{k_{-1}[\mathrm{H_2}]+k_3[\mathrm{H}]+k_{-2}[\mathrm{H_2O}]+k_{58}+k_{59}}\right)[\mathrm{C_{BY5_{FE3}}}]$	
S22 Capping of embedded 5-member ring [75]	**Partially-embedded 5-member ring (eR5) in edge position**
Jump process: 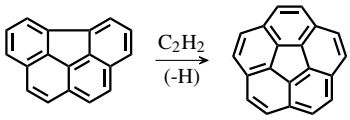 Rate: [b] $\left(k_{71}[\mathrm{C}_s\mathrm{R}_6\mathrm{H}_2]_{\mathrm{ss}}+k_{73}[\mathrm{C}_s\mathrm{R}_6\mathrm{H}-\mathrm{C}_s\mathrm{R}_6]_{\mathrm{ss}}\right)[\mathrm{C_{eR5}}]$	

Process	Parent site
S23 7-member ring growth [50] **(corner partially-embedded five-member ring)**	**Armchair with corner (cRAC) partially-embedded 5-member ring**

Jump process: Rate: [c]

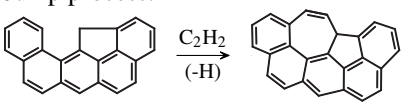

$$\left(k_{85}[C_sR_6H{-}C_sR_6^{\bullet}]_{ss} + k_{89}[C_sR_5H{-}C_sR_6^{\bullet}]_{ss}\right)[C_{cRAC}]$$

S24 7-member ring growth [50] **(partially-embedded 5-member ring)**	**5-member bay ($BY5_{eR5}$) with partially-embedded 5-member ring**

Jump process: Rate: [d]

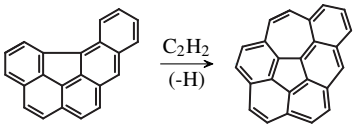

$$\left(k_{77}[C_sR_6H{-}C_sR_6^{\bullet}]_{ss} + k_{81}[C_sR_6H{-}C_sR_6^{\bullet}i]_{ss}\right)[C_{BY5_{eR5}}]$$

S25 7-member bay closure [50] **(partially-embedded 5-member ring 1)**	**7-member bay site 1($BY7_{eR5\text{-}1}$) with partially-embedded 5-member ring**

Jump process: Rate: [e]

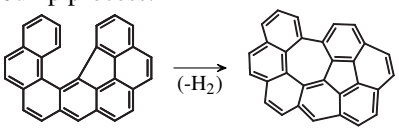

$$\left(k_{92}[C_sR_7{-}C_sR_7{-}H]_{ss} + k_{95}[C_sR_7{-}C_sR_7{-}H_i]_{ss} + k_{100}[C_sR_6H_2{-}C_sR_6H_2]_{ss} + k_{104}[C_sR_6H_2{-}C_sR_6H_2i]_{ss}\right)[C_{BY7_{eR5-1}}]$$

S26 7-member bay closure [50] **(partially-embedded 5-member ring 2)**	**7-member bay site 2($BY7_{eR5\text{-}2}$) with partially-embedded 5-member ring**

Jump process: Rate: [f]

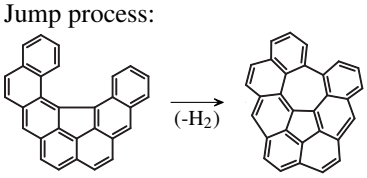

$$\left(k_{107}[C_sR_7{-}C_sR_7{-}H]_{ss} + k_{110}[C_sR_7{-}C_sR_7{-}H_i]_{ss} + k_{115}[C_sR_6H_2{-}C_sR_6H_2]_{ss} + k_{120}[C_sR_6H_2{-}C_sR_6H_2i]_{ss}\right)[C_{BY7_{eR5-2}}]$$

S27 5-7-member ring recombination [this work]	**5-member ring next to 7-member ring (eR5-R7)**

Jump process: Rate: [g]

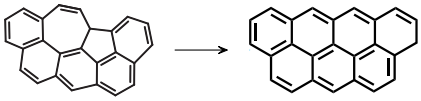

$$\left(k_{139}[C_sR_6H{-}C_sR_6H]_{ss}\right)[C_{eR5-R7}]$$

S28 Free-edge oxidation [this work]	**Two adjacent free-edges (FE2)**

Jump process: Rate: [h]

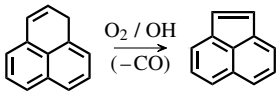

$$\left(k_{125}[C_sR_{6i}{-}O^{\bullet}]_{ss} + k_{126}[C_sR_{6j}{-}O^{\bullet}]_{ss}\right)[C_{FE2}]$$

S29 Free-edge oxidation [this work]	**Free-edge adjacent to non-free-edges (FE_{HACA})**

Jump process: Rate: [i]

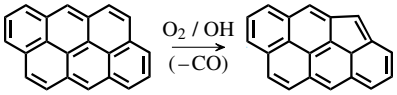

$$2k_{125}[C_sR_6{-}O^{\bullet}]_{ss}[C_{FE_{HACA}}]$$

Process	Parent site
S30 Partially-embedded 5-member ring oxidation [this work]	**Partially-embedded 5-member ring (cR5) in corner position**
Jump process: 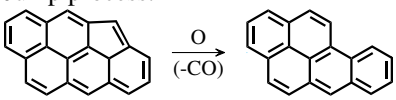	Rate: $(k_{133}+k_{134})\,[\mathrm{C_{cR5}}]$

Notes:

[a] Steady-state intermediates vector V_{ss} and partial-equilibrium intermediates vector V_{peq} defined as:
$V_{\mathrm{ss}} = \{\mathrm{C}_s\mathrm{R}_6{}^{\bullet}, \mathrm{C}_s\mathrm{R}_6{-}\mathrm{C}_2\mathrm{H}_2, \mathrm{C}_s\mathrm{R}_6{-}\mathrm{C}_2\mathrm{H}, \mathrm{C}_s\mathrm{R}_6{-}\mathrm{C}_2\mathrm{H}_3, \mathrm{C}_s\mathrm{R}_6{-}\mathrm{C}_2\mathrm{H}_3{}^{\bullet}, \mathrm{C}_s\mathrm{R}_6(\mathrm{C}_2\mathrm{H})(\mathrm{C}_2\mathrm{H}_3), \mathrm{C}_s\mathrm{R}_6{-}\mathrm{R}_6{}^{\bullet}, \mathrm{C}_s\mathrm{R}_6{-}\mathrm{R}_6\}$
$V_{\mathrm{peq}} = \{\mathrm{C}_s\mathrm{R}_6{}^{\bullet}, \mathrm{C}_s\mathrm{R}_6{-}\mathrm{C}_2\mathrm{H}_2, \mathrm{C}_s\mathrm{R}_6{-}\mathrm{C}_2\mathrm{H}, \mathrm{C}_s\mathrm{R}_6{-}\mathrm{C}_2\mathrm{H}_3, \mathrm{C}_s\mathrm{R}_6{-}\mathrm{C}_2\mathrm{H}_3{}^{\bullet}, \mathrm{C}_s\mathrm{R}_6(\mathrm{C}_2\mathrm{H})(\mathrm{C}_2\mathrm{H}_3)\}$
Rate calculated as per Leon et al. [49]: $\dot{r}_{S1} = \dot{r}_{S1,\mathrm{ss}}$ if $\dot{r}_{S1,\mathrm{peq}} > \dot{r}_{S3}$, $\dot{r}_{S1} = \dot{r}_{S1,\mathrm{peq}}$ o.w.

[b] Steady-state intermediates vector V_{ss} defined as:
$V_{\mathrm{ss}} = \{\mathrm{C}_s\mathrm{R}_6{}^{\bullet}, \mathrm{C}_s\mathrm{R}_6{-}\mathrm{C}_2\mathrm{H}_2, \mathrm{C}_s\mathrm{R}_6{}^{\bullet}{-}\mathrm{C}_2\mathrm{H}_3, \mathrm{C}_s\mathrm{R}_6{-}\mathrm{H}_2, \mathrm{C}_s\mathrm{R}_6\mathrm{H}{-}\mathrm{C}_s\mathrm{R}_6\}$

[c] Steady-state intermediates vector V_{ss} defined as:
$V_{\mathrm{ss}} = \{\mathrm{C}_s\mathrm{R}_6{}^{\bullet}, \mathrm{C}_s\mathrm{R}_6{-}\mathrm{C}_2\mathrm{H}_2, \mathrm{C}_s\mathrm{R}_6\mathrm{H}{-}\mathrm{C}_s\mathrm{R}_6{}^{\bullet}, \mathrm{C}_s\mathrm{R}_5{}^{\bullet}, \mathrm{C}_s\mathrm{R}_5{-}\mathrm{C}_2\mathrm{H}_2, \mathrm{C}_s\mathrm{R}_5\mathrm{H}{-}\mathrm{C}_s\mathrm{R}_6{}^{\bullet}\}$

[d] Steady-state intermediates vector V_{ss} defined as:
$V_{\mathrm{ss}} = \{\mathrm{C}_s\mathrm{R}_6{}^{\bullet}, \mathrm{C}_s\mathrm{R}_6{-}\mathrm{C}_2\mathrm{H}_2, \mathrm{C}_s\mathrm{R}_6\mathrm{H}{-}\mathrm{C}_s\mathrm{R}_6{}^{\bullet}, \mathrm{C}_s\mathrm{R}_6{}^{\bullet}{}_i, \mathrm{C}_s\mathrm{R}_6{-}\mathrm{C}_2\mathrm{H}_{2i}, \mathrm{C}_s\mathrm{R}_6\mathrm{H}{-}\mathrm{C}_s\mathrm{R}_6{}^{\bullet}{}_i\}$

[e] Steady-state intermediates vector V_{ss} defined as:
$V_{\mathrm{ss}} = \{\mathrm{C}_s\mathrm{R}_6{}^{\bullet}, \mathrm{C}_s\mathrm{R}_7{-}\mathrm{R}_7{-}\mathrm{H}, \mathrm{C}_s\mathrm{R}_6{}^{\bullet}{}_i, \mathrm{C}_s\mathrm{R}_7{-}\mathrm{R}_7{-}\mathrm{H}_i, \mathrm{C}_s\mathrm{R}_6{}^{2\bullet}, \mathrm{C}_s\mathrm{R}_7\mathrm{H}{-}\mathrm{C}_s\mathrm{R}_7, \mathrm{C}_s\mathrm{R}_7\mathrm{H}{-}\mathrm{C}_s\mathrm{R}_6\mathrm{H}, \mathrm{C}_s\mathrm{R}_6{}^{2\bullet}{}_i, \mathrm{C}_s\mathrm{R}_7\mathrm{H}{-}\mathrm{C}_s\mathrm{R}_{7i}, \mathrm{C}_s\mathrm{R}_7\mathrm{H}{-}\mathrm{C}_s\mathrm{R}_6\mathrm{H}_i\}$

[f] Steady-state intermediates vector V_{ss} defined as:
$V_{\mathrm{ss}} = \{\mathrm{C}_s\mathrm{R}_6{}^{\bullet}, \mathrm{C}_s\mathrm{R}_7{-}\mathrm{R}_7{-}\mathrm{H}, \mathrm{C}_s\mathrm{R}_6{}^{\bullet}{}_i, \mathrm{C}_s\mathrm{R}_7{-}\mathrm{R}_7{-}\mathrm{H}_i, \mathrm{C}_s\mathrm{R}_6{}^{2\bullet}, \mathrm{C}_s\mathrm{R}_7\mathrm{H}{-}\mathrm{C}_s\mathrm{R}_7, \mathrm{C}_s\mathrm{R}_7\mathrm{H}{-}\mathrm{C}_s\mathrm{R}_6\mathrm{H}, \mathrm{C}_s\mathrm{R}_6{}^{2\bullet}{}_i, \mathrm{C}_s\mathrm{R}_7\mathrm{H}{-}\mathrm{C}_s\mathrm{R}_{7i}, \mathrm{C}_s\mathrm{R}_7\mathrm{H}{-}\mathrm{C}_s\mathrm{R}_6\mathrm{H}_i\}$

[g] Steady-state intermediates vector V_{ss} defined as:
$V_{\mathrm{ss}} = \{\mathrm{C}_s\mathrm{R}_7\mathrm{H}_2{-}\mathrm{C}_s\mathrm{R}_5, \mathrm{C}_s\mathrm{R}_7\mathrm{H}{-}\mathrm{C}_s\mathrm{R}_5\mathrm{H}, \mathrm{C}_s\mathrm{R}_3\mathrm{H}{-}\mathrm{C}_s\mathrm{R}_3\mathrm{H}, \mathrm{C}_s\mathrm{R}_6\mathrm{H}{-}\mathrm{C}_s\mathrm{R}_6\mathrm{H}\}$

[h] Steady-state intermediates vector V_{ss} defined as:
$V_{\mathrm{ss}} = \{\mathrm{C}_s\mathrm{R}_{6i}{}^{\bullet}, \mathrm{C}_s\mathrm{R}_{6j}{}^{\bullet}, \mathrm{C}_s\mathrm{R}_{6i}{-}\mathrm{O}^{\bullet}, \mathrm{C}_s\mathrm{R}_{6j}{-}\mathrm{O}^{\bullet}, \mathrm{C}_s\mathrm{R}_{6i}{-}\mathrm{OH}, \mathrm{C}_s\mathrm{R}_6\mathrm{j}{-}\mathrm{OH}\}$

[i] Steady-state intermediates vector V_{ss} defined as:
$V_{\mathrm{ss}} = \{\mathrm{C}_s\mathrm{R}_6{}^{\bullet}, \mathrm{C}_s\mathrm{R}_6{-}\mathrm{O}^{\bullet}, \mathrm{C}_s\mathrm{R}_6{-}\mathrm{OH}\}$

References

[1] J. Appel, H. Bockhorn, and M. Frenklach. Kinetic modeling of soot formation with detailed chemistry and physics: laminar premixed flames of C_2 hydrocarbons. *Combust. Flame*, 121(1):122 – 136, 2000. doi:10.1016/S0010-2180(99)00135-2.

[2] M. Baradyn and A. Ratkiewicz. Kinetics of the Hydrogen abstraction PAH + •OH → PAH Radical + H_2O Reaction Class: An Application of the Reaction Class Transition State Theory (RC-TST) and Structure–Activity Relationship (SAR). *J. Phys. Chem. A*, 123(4):750–763, 2019. doi:10.1021/acs.jpca.8b10988.

[3] M. Baroncelli, Q. Mao, S. Galle, N. Hansen, and H. Pitsch. Role of ring-enlargement reactions in the formation of aromatic hydrocarbons. *Phys. Chem. Chem. Phys.*, 22:4699–4714, 2020. doi:10.1039/C9CP05854K.

[4] E. Bertin, A. Münzer, S. Reichenberger, R. Streubel, T. Vinnay, H. Wiggers, C. Schulz, S. Barcikowski, and G. Marzun. Durability study of platinum nanoparticles supported on gas-phase synthesized graphene in oxygen reduction reaction conditions. *Appl. Surf. Sci.*, 467-468:1181–1186, 2019. doi:10.1016/j.apsusc.2018.10.061.

[5] J. Bittner and J. Howard. Composition profiles and reaction mechanisms in a near-sooting premixed benzene/oxygen/argon flame. *Symp. (Int.) Combust.*, 18(1): 1105–1116, 1981. doi:10.1016/S0082-0784(81)80115-4. Eighteenth Symposium (International) on Combustion.

[6] N. Bundaleska, D. Tsyganov, A. Dias, E. Felizardo, J. Henriques, F. M. Dias, M. Abrashev, J. Kissovski, and E. Tatarova. Microwave plasma enabled synthesis of free standing carbon nanostructures at atmospheric pressure conditions. *Phys. Chem. Chem. Phys.*, 20:13810–13824, 2018. doi:10.1039/C8CP01896K.

[7] J. Camacho, Y. Tao, and H. Wang. Kinetics of nascent soot oxidation by molecular oxygen in a flow reactor. *Proc. Combust. Inst.*, 35(2):1887 – 1894, 2015. doi:10.1016/j.proci.2014.05.095.

[8] X.-M. Cao, Z.-R. Li, J.-B. Wang, and X.-Y. Li. Rate rules for hydrogen abstraction reaction kinetics of polycyclic aromatic hydrocarbons and vinyl radical. *Theor. Chem. Acc.*, 139(6):94, 2020. doi:10.1007/s00214-020-02612-0.

[9] M. Celnik, A. Raj, R. West, R. Patterson, and M. Kraft. Aromatic site description of soot particles. *Combust. Flame*, 155(1-2):161–180, 2008. doi:10.1016/j.combustflame.2008.04.011.

[10] G. Churilov, P. Novikov, V. Tarabanko, V. Lopatin, N. Vnukova, and N. Bulina. On the mechanism of fullerene formation in a carbon plasma. *Carbon*, 40(6):891–896, 2002. doi:10.1016/S0008-6223(01)00211-1.

[11] M. Commodo, K. Kaiser, G. D. Falco, P. Minutolo, F. Schulz, A. D'Anna, and L. Gross. On the early stages of soot formation: Molecular structure elucidation by high-resolution atomic force microscopy. *Combust. Flame*, 205:154–164, 2019. doi:10.1016/j.combustflame.2019.03.042.

[12] Computational Modelling Group. MOpS Particle Simulator. `https://github.com/ucam-ceb-como/MOpS`, 2021. Commit: 404e1504c65bfb0a3f02d238bfac8be728073233.

[13] J. Coro, M. Suárez, L. S. Silva, K. I. Eguiluz, and G. R. Salazar-Banda. Fullerene applications in fuel cells: A review. *Int. J. Hydrog. Energy*, 41(40):17944–17959, 2016. doi:10.1016/j.ijhydene.2016.08.043.

[14] A. D'Anna and J. Kent. A model of particulate and species formation applied to laminar, nonpremixed flames for three aliphatic-hydrocarbon fuels. *Combust. Flame*, 152(4):573–587, 2008. doi:10.1016/j.combustflame.2007.08.003.

[15] A. Dato. Graphene synthesized in atmospheric plasmas—a review. *J. Mater. Res.*, 34(1):214–230, 2019. doi:10.1557/jmr.2018.470.

[16] A. Dato and M. Frenklach. Substrate-free microwave synthesis of graphene: experimental conditions and hydrocarbon precursors. *New J. Phys.*, 12(12):125013, 2010. doi:10.1088/1367-2630/12/12/125013.

[17] A. Dato, V. Radmilovic, Z. Lee, J. Phillips, and M. Frenklach. Substrate-free gas-phase synthesis of graphene sheets. *Nano Letters*, 8(7):2012–2016, 2008. doi:10.1021/nl8011566.

[18] F. Defoeux, V. Dias, C. Renard, P. Van Tiggelen, and J. Vandooren. Experimental investigation of the structure of a sooting premixed benzene/oxygen/argon flame burning at low pressure. *Proc. Combust. Inst.*, 30(1):1407–1415, 2005. doi:10.1016/j.proci.2004.08.014.

[19] D. E. Edwards, D. Y. Zubarev, W. A. Lester, and M. Frenklach. Pathways to soot oxidation: Reaction of OH with phenanthrene radicals. *J. Phys. Chem. A*, 118(37): 8606–8613, 2014. doi:10.1021/jp5033178.

[20] P. Elvati, V. Dillstrom, and A. Violi. Oxygen driven soot formation. *Proc. Combust. Inst.*, 36(1):825–832, 2017. doi:10.1016/j.proci.2016.09.019.

[21] C. P. Fenimore and G. W. Jones. Oxidation of soot by hydroxyl radicals. *J. Phys. Chem.*, 71(3):593–597, 1967. doi:10.1021/j100862a021.

[22] M. Frenklach. Reaction mechanism of soot formation in flames. *Phys. Chem. Chem. Phys.*, 4:2028–2037, 2002. doi:10.1039/B110045A.

[23] M. Frenklach and H. Wang. Detailed modeling of soot particle nucleation and growth. *Symp. (Int.) Combust.*, 23(1):1559 – 1566, 1991. doi:10.1016/S0082-0784(06)80426-1. Twenty-Third Symposium (International) on Combustion.

[24] M. Frenklach, C. A. Schuetz, and J. Ping. Migration mechanism of aromatic-edge growth. *Proc. Combust. Inst.*, 30(1):1389–1396, 2005. doi:10.1016/j.proci.2004.07.048.

[25] M. Frenklach, Z. Liu, R. I. Singh, G. R. Galimova, V. N. Azyazov, and A. M. Mebel. Detailed, sterically-resolved modeling of soot oxidation: Role of O atoms, interplay with particle nanostructure, and emergence of inner particle burning. *Combust. Flame*, 188:284–306, 2018. doi:10.1016/j.combustflame.2017.10.012.

[26] M. Frenklach, R. I. Singh, and A. M. Mebel. On the low-temperature limit of HACA. *Proc. Combust. Inst.*, 37(1):969–976, 2019. doi:10.1016/j.proci.2018.05.068.

[27] H. Ghiassi, I. C. Jaramillo, and J. S. Lighty. Kinetics of soot oxidation by molecular oxygen in a premixed flame. *Energy Fuels*, 30(4):3463–3472, 2016. doi:10.1021/acs.energyfuels.5b02942.

[28] H. Ghiassi, D. Lignell, and J. S. Lighty. Soot oxidation by OH: Theory development, model, and experimental validation. *Energy Fuels*, 31(3):2236–2245, 2017. doi:10.1021/acs.energyfuels.6b02193.

[29] S. Goodarzi, T. Da Ros, J. Conde, F. Sefat, and M. Mozafari. Fullerene: biomedical engineers get to revisit an old friend. *Mater. Today*, 20(8):460–480, 2017. doi:10.1016/j.mattod.2017.03.017.

[30] H. Guo, P. M. Anderson, and P. B. Sunderland. Optimized rate expressions for soot oxidation by OH and O_2. *Fuel*, 172:248 – 252, 2016. doi:10.1016/j.fuel.2016.01.030.

[31] L. B. Harding, Y. Georgievskii, and S. J. Klippenstein. Predictive theory for Hydrogen atom-Hydrocarbon radical association kinetics. *J. Phys. Chem. A*, 109(21): 4646–4656, 2005. doi:10.1021/jp0508608.

[32] P. Hebgen, A. Goel, J. B. Howard, L. C. Rainey, and J. B. Vander Sande. Synthesis of fullerenes and fullerenic nanostructures in a low-pressure benzene/oxygen diffusion flame. *Proc. Combust. Inst.*, 28(1):1397 – 1404, 2000. doi:10.1016/S0082-0784(00)80355-0.

[33] K. J. Higgins, H. Jung, D. B. Kittelson, J. T. Roberts, and M. R. Zachariah. Size-selected nanoparticle chemistry: Kinetics of soot oxidation. *J. Phys. Chem. A*, 106 (1):96–103, 2002. doi:10.1021/jp004466f.

[34] K.-H. Homann. Fullerenes and soot formation— new pathways to large particles in flames. *Angew. Chem. Int. Ed. Engl.*, 37(18):2434–2451, 1998. doi:10.1002/(SICI)1521-3773(19981002)37:18<2434::AID-ANIE2434>3.0.CO;2-L.

[35] D. Hou and X. You. Reaction kinetics of hydrogen abstraction from polycyclic aromatic hydrocarbons by H atoms. *Phys. Chem. Chem. Phys.*, 19:30772–30780, 2017. doi:10.1039/C7CP04964A.

[36] J. B. Howard. Fullerenes formation in flames. *Symp. (Int.) Combust.*, 24(1):933 – 946, 1992. doi:10.1016/S0082-0784(06)80111-6. Twenty-Fourth Symposium on Combustion.

[37] J. B. Howard, A. L. Lafleur, Y. Makarovsky, S. Mitra, C. J. Pope, and T. K. Yadav. Fullerenes synthesis in combustion. *Carbon*, 30(8):1183 – 1201, 1992. doi:10.1016/0008-6223(92)90061-Z. Special Issue on Fullerenes.

[38] J. B. Howard, J. T. McKinnon, M. E. Johnson, Y. Makarovsky, and A. L. Lafleur. Production of C_{60} and C_{70} fullerenes in benzene-oxygen flames. *J. Phys. Chem.*, 96(16):6657–6662, 1992. doi:10.1021/j100195a026.

[39] M. Jiménez, R. Rincón, A. Marinas, and M. Calzada. Hydrogen production from ethanol decomposition by a microwave plasma: Influence of the plasma gas flow. *Int. J. Hydrog. Energy*, 38(21):8708 – 8719, 2013. doi:10.1016/j.ijhydene.2013.05.004.

[40] K. Johansson, M. Head-Gordon, P. Schrader, K. Wilson, and H. Michelsen. Resonance-stabilized hydrocarbon-radical chain reactions may explain soot inception and growth. *Science*, 361(6406):997–1000, 2018.

[41] Y. Ju and W. Sun. Plasma assisted combustion: Dynamics and chemistry. *Prog. Energy Combust. Sci.*, 48:21–83, 2015. doi:10.1016/j.pecs.2014.12.002.

[42] A. Keller, R. Kovacs, and K.-H. Homann. Large molecules, ions, radicals and small soot particles in fuel-rich hydrocarbon flames. Part IV. Large polycyclic aromatic hydrocarbons and their radicals in a fuel-rich benzene–oxygen flame. *Phys. Chem. Chem. Phys.*, 2:1667–1675, 2000. doi:10.1039/A908190I.

[43] C. Kim, A. El-Leathy, F. Xu, and G. Faeth. Soot surface growth and oxidation in laminar diffusion flames at pressures of 0.1–1.0 atm. *Combust. Flame*, 136(1):191 – 207, 2004. doi:10.1016/j.combustflame.2003.09.017.

[44] V. V. Kislov and A. M. Mebel. The formation of naphthalene, azulene, and fulvalene from cyclic C_5 species in combustion: An ab initio/RRKM study of 9-H-Fulvalenyl (C_5H_5–C_5H_4) radical rearrangements. *J. Phys. Chem. A*, 111(38):9532–9543, 2007. doi:10.1021/jp0732099.

[45] V. V. Kislov, N. I. Islamova, A. M. Kolker, S. H. Lin, and A. M. Mebel. Hydrogen abstraction acetylene addition and Diels-Alder mechanisms of PAH formation: A detailed study using first principles calculations. *J. Chem. Theory Comput.*, 1(5): 908–924, 2005. doi:10.1021/ct0500491.

[46] S. J. Klippenstein, L. B. Harding, and Y. Georgievskii. On the formation and decomposition of C_7H_8. *Proc. Combust. Inst.*, 31(1):221 – 229, 2007. doi:10.1016/j.proci.2006.08.045.

[47] J. Y. W. Lai, P. Elvati, and A. Violi. Stochastic atomistic simulation of polycyclic aromatic hydrocarbon growth in combustion. *Phys. Chem. Chem. Phys.*, 16:7969–7979, 2014. doi:10.1039/C4CP00112E.

[48] R. Larciprete, P. Lacovig, S. Gardonio, A. Baraldi, and S. Lizzit. Atomic oxygen on graphite: Chemical characterization and thermal reduction. *J. Phys. Chem. C*, 116(18):9900–9908, 2012. doi:10.1021/jp2098153.

[49] G. Leon, N. Eaves, J. Akroyd, S. Mosbach, and M. Kraft. A new methodology to calculate process rates in a Kinetic Monte Carlo model of PAH growth. *Combust. Flame*, 209:133–143, 2019. doi:10.1016/j.combustflame.2019.07.032.

[50] G. Leon, A. Menon, L. Pascazio, E. J. Bringley, J. Akroyd, and M. Kraft. Kinetic Monte Carlo statistics of curvature integration by HACA growth and bay closure reactions for PAH growth in a counterflow diffusion flame. *Proc. Combust. Inst.*, 2020. doi:10.1016/j.proci.2020.06.352.

[51] Y. A. Levendis and R. C. Flagan. Combustion of uniformly sized glassy carbon particles. *Combust. Sci. Technol.*, 53(2-3):117–136, 1987. doi:10.1080/00102208708947023.

[52] P. Liu, H. Lin, Y. Yang, C. Shao, C. Gu, and Z. Huang. New insights into thermal decomposition of polycyclic aromatic hydrocarbon oxyradicals. *J. Phys. Chem. A*, 118(48):11337–11345, 2014. doi:10.1021/jp510498j.

[53] N. M. Marinov. A detailed chemical kinetic model for high temperature ethanol oxidation. *Int. J. Chem. Kinet.*, 31(3):183–220, 1999. doi:10.1002/(SICI)1097-4601(1999)31:3<183::AID-KIN3>3.0.CO;2-X.

[54] J. W. Martin, D. Hou, A. Menon, L. Pascazio, J. Akroyd, X. You, and M. Kraft. Reactivity of polycyclic aromatic hydrocarbon soot precursors: Implications of localized π-radicals on rim-based pentagonal rings. *J. Phys. Chem. C*, 123(43): 26673–26682, 2019. doi:10.1021/acs.jpcc.9b07558.

[55] J. T. McKinnon. *Chemical and physical mechanisms of soot formation*. PhD thesis, Massachusetts Institute of Technology, 1989.

[56] A. M. Mebel, Y. Georgievskii, A. W. Jasper, and S. J. Klippenstein. Temperature- and pressure-dependent rate coefficients for the HACA pathways from benzene to naphthalene. *Proc. Combust. Inst.*, 36(1):919–926, 2017. doi:10.1016/j.proci.2016.07.013.

[57] A. Menon, G. Leon, J. Akroyd, and M. Kraft. A density functional theory study on the kinetics of seven-member ring formation in polyaromatic hydrocarbons. *Combust. Flame*, 217:152–174, 2020. doi:10.1016/j.combustflame.2020.03.032.

[58] A. Menon, J. Martin, G. Leon, D. Hou, L. Pascazio, X. You, and M. Kraft. Reactive localized π-radicals on rim-based pentagonal rings: Properties and concentration in flames. *Proc. Combust. Inst.*, 2020. doi:10.1016/j.proci.2020.07.042.

[59] A. Menon, J. W. Martin, J. Akroyd, and M. Kraft. Reactivity of polycyclic aromatic hydrocarbon soot precursors: Kinetics and equilibria. *J. Phys. Chem. A*, 124(48): 10040–10052, 2020. doi:10.1021/acs.jpca.0c07811.

[60] J. Molina. Graphene-based fabrics and their applications: a review. *RSC Adv.*, 6: 68261–68291, 2016. doi:10.1039/C6RA12365A.

[61] A. Münzer, L. Xiao, Y. H. Sehlleier, C. Schulz, and H. Wiggers. All gas-phase synthesis of graphene: Characterization and its utilization for silicon-based lithium-ion batteries. *Electrochim. Acta*, 272:52–59, 2018. doi:10.1016/j.electacta.2018.03.137.

[62] A. Nag, A. Mitra, and S. C. Mukhopadhyay. Graphene and its sensor-based applications: A review. *Sens. Actuators A: Phys.*, 270:177–194, 2018. doi:10.1016/j.sna.2017.12.028.

[63] K. Narayanaswamy, G. Blanquart, and H. Pitsch. A consistent chemical mechanism for oxidation of substituted aromatic species. *Combust. Flame*, 157(10):1879–1898, 2010. doi:10.1016/j.combustflame.2010.07.009.

[64] A. Naseri, A. D. Sediako, F. Liu, M. Barati, R. D. Baker, and M. J. Thomson. In-situ studies of O_2 and O radical oxidation of carbon black using thermogravimetric analysis and environmental transmission electron microscopy. *Carbon*, 156:299–308, 2020. doi:10.1016/j.carbon.2019.09.039.

[65] M. Nayebzadeh, M. Vahedpour, A. Shiroudi, and J. M. Rius-Bartra. Kinetics and oxidation mechanism of pyrene initiated by hydroxyl radical. A theoretical investigation. *Chem. Phys.*, 528:110522, 2020. doi:10.1016/j.chemphys.2019.110522.

[66] K. Neoh, J. Howard, and A. Sarofim. Effect of oxidation on the physical structure of soot. *Symp. (Int.) Combust.*, 20(1):951–957, 1985. doi:10.1016/S0082-0784(85)80584-1. Twentieth Symposium (International) on Combustion.

[67] K. G. Neoh. *Soot burnout in flames*. PhD thesis, Massachusetts Institute of Technology, 1981.

[68] K. G. Neoh, J. B. Howard, and A. F. Sarofim. Soot oxidation in flames. In D. C. Siegla and G. W. Smith, editors, *Particulate Carbon: Formation During Combustion*, pages 261–282. Springer US, Boston, MA, 1981. doi:10.1007/978-1-4757-6137-5_9.

[69] R. Ono. Optical diagnostics of reactive species in atmospheric-pressure nonthermal plasma. *J. Phys. D: Appl. Phys.*, 49(8):083001, 2016. doi:10.1088/0022-3727/49/8/083001.

[70] S. Park and R. S. Ruoff. Chemical methods for the production of graphenes. *Nature Nanotech.*, 4(4):217–224, Apr 2009. doi:10.1038/nnano.2009.58.

[71] L. Pascazio, J. W. Martin, A. Menon, D. Hou, X. You, and M. Kraft. Aromatic penta-linked hydrocarbons in soot nanoparticle formation. *Proc. Combust. Inst.*, 2020. doi:10.1016/j.proci.2020.09.029.

[72] F. Pedregosa, G. Varoquaux, A. Gramfort, V. Michel, B. Thirion, O. Grisel, M. Blondel, P. Prettenhofer, R. Weiss, V. Dubourg, J. Vanderplas, A. Passos, D. Cournapeau, M. Brucher, M. Perrot, and E. Duchesnay. Scikit-learn: Machine learning in Python. *J. Mac. Learn. Res.*, 12:2825–2830, 2011.

[73] S. J. Pendleton, A. Montello, C. Carter, W. Lempert, and M. A. Gundersen. Vibrational and rotational CARS measurements of nitrogen in afterglow of streamer discharge in atmospheric pressure fuel/air mixtures. *J. Phys. D: Appl. Phys.*, 45 (49):495401, 2012. doi:10.1088/0022-3727/45/49/495401.

[74] S. J. Pendleton, S. Bowman, C. Carter, M. A. Gundersen, and W. Lempert. The production and evolution of atomic oxygen in the afterglow of streamer discharge in atmospheric pressure fuel/air mixtures. *J. Phys. D: Appl. Phys.*, 46(30):305202, 2013. doi:10.1088/0022-3727/46/30/305202.

[75] A. Raj. Structural effects on the growth of large polycyclic aromatic hydrocarbons by C_2H_2. *Combust. Flame*, 204:331–340, 2019. doi:10.1016/j.combustflame.2019.03.027.

[76] A. Raj, M. Celnik, R. Shirley, M. Sander, R. Patterson, R. West, and M. Kraft. A statistical approach to develop a detailed soot growth model using PAH characteristics. *Combust. Flame*, 156(4):896–913, 2009. doi:10.1016/j.combustflame.2009.01.005.

[77] A. Raj, P. L. Man, T. S. Totton, M. Sander, R. A. Shirley, and M. Kraft. New polycyclic aromatic hydrocarbon (PAH) surface processes to improve the model prediction of the composition of combustion-generated PAHs and soot. *Carbon*, 48(2):319 – 332, 2010. doi:10.1016/j.carbon.2009.09.030.

[78] H. Richter, S. Granata, W. H. Green, and J. B. Howard. Detailed modeling of PAH and soot formation in a laminar premixed benzene/oxygen/argon low-pressure flame. *Proc. Combust. Inst.*, 30(1):1397–1405, 2005. doi:j.proci.2004.08.088.

[79] S. P. Roy and D. C. Haworth. A systematic comparison of detailed soot models and gas-phase chemical mechanisms in laminar premixed flames. *Combust. Sci. Technol.*, 188(7):1021–1053, 2016. doi:10.1080/00102202.2016.1145117.

[80] M. Salamanca, M. Sirignano, M. Commodo, P. Minutolo, and A. D'Anna. The effect of ethanol on the particle size distributions in ethylene premixed flames. *Exp. Therm. Fluid Sci.*, 43:71–75, 2012. doi:10.1016/j.expthermflusci.2012.04.006. Seventh Mediterranean Combustion Symposium.

[81] J. C. Saldinger, Q. Wang, P. Elvati, and A. Violi. Characterizing the diversity of aromatics in a coflow diffusion Jet A-1 surrogate flame. *Fuel*, 268:117198, 2020. doi:10.1016/j.fuel.2020.117198.

[82] A. S. Semenikhin, A. S. Savchenkova, I. V. Chechet, S. G. Matveev, Z. Liu, M. Frenklach, and A. M. Mebel. Rate constants for H abstraction from benzo(a)pyrene and chrysene: A theoretical study. *Phys. Chem. Chem. Phys.*, 19: 25401–25413, 2017. doi:10.1039/C7CP05560A.

[83] M. Singh, A. Sengupta, K. Zeller, G. Skoptsov, and R. L. Vander Wal. Effect of hydrogen concentration on graphene synthesis using microwave-driven plasma-mediated methane cracking. *Carbon*, 143:802–813, 2019. doi:10.1016/j.carbon.2018.11.082.

[84] R. Singh and M. Frenklach. A mechanistic study of the influence of graphene curvature on the rate of high-temperature oxidation by molecular oxygen. *Carbon*, 101:203–212, 2016. doi:10.1016/j.carbon.2016.01.090.

[85] R. I. Singh, A. M. Mebel, and M. Frenklach. Oxidation of graphene-edge six- and five-member rings by molecular oxygen. *J. Phys. Chem. A*, 119(28):7528–7547, 2015. doi:10.1021/acs.jpca.5b00868.

[86] E. Tatarova, F. M. Dias, E. Felizardo, J. Henriques, C. M. Ferreira, and B. Gordiets. Microwave plasma torches driven by surface waves. *Plasma Sources Sci. Technol.*, 17(2):024004, 2008. doi:10.1088/0963-0252/17/2/024004.

[87] E. Tatarova, J. P. Henriques, E. Felizardo, M. Lino da Silva, C. M. Ferreira, and B. Gordiets. Microwave plasma source operating with atmospheric pressure air-water mixtures. *J. Appl. Phys.*, 112(9):093301, 2012. doi:10.1063/1.4762015.

[88] E. Tatarova, J. Henriques, C. C. Luhrs, A. Dias, J. Phillips, M. V. Abrashev, and C. M. Ferreira. Microwave plasma based single step method for free standing graphene synthesis at atmospheric conditions. *Appl. Phys. Lett.*, 103(13):134101, 2013. doi:10.1063/1.4822178.

[89] E. Tatarova, A. Dias, J. Henriques, A. M. B. do Rego, A. M. Ferraria, M. V. Abrashev, C. C. Luhrs, J. Phillips, F. M. Dias, and C. M. Ferreira. Microwave plasmas applied for the synthesis of free standing graphene sheets. *J. Phys. D: Appl. Phys.*, 47(38):385501, 2014. doi:10.1088/0022-3727/47/38/385501.

[90] H. Terrones and M. Terrones. Curved nanostructured materials. *New J. Phys.*, 5: 126–126, oct 2003. doi:10.1088/1367-2630/5/1/126.

[91] A. Violi. Cyclodehydrogenation reactions to cyclopentafused polycyclic aromatic hydrocarbons. *J. Phys. Chem. A*, 109(34):7781–7787, 2005. doi:10.1021/jp052384r.

[92] J. Walls and R. Strickland-Constable. Oxidation of carbon between 1000–2400°C. *Carbon*, 1(3):333 – 338, 1964. doi:10.1016/0008-6223(64)90288-X.

[93] C. Wang, Z. Lu, J. Ma, X. Chen, C. Yang, and W. Xia. Pressure-dependent synthesis of graphene nanoflakes using $Ar/H_2/CH_4$ non-thermal plasma based on rotating arc discharge. *Diam. Relat. Mater.*, 111:108176, 2021. doi:10.1016/j.diamond.2020.108176.

[94] H. Wang. Formation of nascent soot and other condensed-phase materials in flames. *Proc. Combust. Inst.*, 33(1):41 – 67, 2011. doi:10.1016/j.proci.2010.09.009.

[95] H. Wang and M. Frenklach. Calculations of rate coefficients for the chemically activated reactions of acetylene with vinylic and aromatic radicals. *J. Phys. Chem.*, 98(44):11465–11489, 1994. doi:10.1021/j100095a033.

[96] Q. Wang, P. Elvati, D. Kim, K. O. Johansson, P. E. Schrader, H. A. Michelsen, and A. Violi. Spatial dependence of the growth of polycyclic aromatic compounds in an ethylene counterflow flame. *Carbon*, 149:328–335, 2019. doi:10.1016/j.carbon.2019.03.017.

[97] Q. Wang, J. C. Saldinger, P. Elvati, and A. Violi. Insights on the effect of ethanol on the formation of aromatics. *Fuel*, 264:116773, 2020. doi:10.1016/j.fuel.2019.116773.

[98] M. L. Waskom. seaborn: statistical data visualization. *J. Open Source Softw.*, 6 (60):3021, 2021. doi:10.21105/joss.03021.

[99] A. Y. Watson and P. A. Valberg. Carbon black and soot: Two different substances. *AIHAJ - Am. Ind. Hyg. Assoc.*, 62(2):218–228, 2001. doi:10.1080/15298660108984625.

[100] P. Weilmünster, A. Keller, and K.-H. Homann. Large molecules, radicals, ions, and small soot particles in fuel-rich hydrocarbon flames: Part I: positive ions of polycyclic aromatic hydrocarbons(PAH) in low-pressure premixed flames of acetylene and oxygen. *Combust. Flame*, 116(1):62 – 83, 1999. doi:10.1016/S0010-2180(98)00049-2.

[101] P. R. Westmoreland. *Experimental and theoretical analysis of oxidation and growth chemistry in a fuel-rich acetylene flame*. PhD thesis, Massachusetts Institute of Technology, 1986.

[102] R. Whitesides and M. Frenklach. Detailed Kinetic Monte Carlo simulations of graphene-edge growth. *J. Phys. Chem. A*, 114(2):689–703, 2010. doi:10.1021/jp906541a.

[103] R. Whitesides, D. Domin, R. Salomón-Ferrer, W. A. Lester, and M. Frenklach. Graphene layer growth chemistry: Five- and six-member ring flip reaction. *J. Phys. Chem. A*, 112(10):2125–2130, 2008. doi:10.1021/jp075785a.

[104] R. Whitesides, D. Domin, R. Salomón-Ferrer, W. A. Lester, and M. Frenklach. Embedded-ring migration on graphene zigzag edge. *Proc. Combust. Inst.*, 32(1): 577 – 583, 2009. doi:10.1016/j.proci.2008.06.096.

[105] E. K. Yapp, C. G. Wells, J. Akroyd, S. Mosbach, R. Xu, and M. Kraft. Modelling PAH curvature in laminar premixed flames using a detailed population balance model. *Combust. Flame*, 176:172–180, 2017. doi:10.1016/j.combustflame.2016.10.004.

[106] X. You, R. Whitesides, D. Zubarev, W. A. Lester, and M. Frenklach. Bay-capping reactions: Kinetics and influence on graphene-edge growth. *Proc. Combust. Inst.*, 33(1):685–692, 2011. doi:10.1016/j.proci.2010.05.110.